ELSEVIER

Chemical Geology 188 (2002) 193–215

CHEMICAL GEOLOGY
INCLUDING
ISOTOPE GEOSCIENCE

www.elsevier.com/locate/chemgeo

Interpretation of monazite ages obtained via in situ analysis

E.J. Catlos [a,*], L.D. Gilley [b], T. Mark Harrison [c]

[a] *School of Geology, Oklahoma State University, Stillwater, OK, 74078, USA*
[b] *Department of Geology, University of Kansas, Lawrence, KS, 66045-7613, USA*
[c] *Research School of Earth Sciences, The Australian National University Canberra, A.C.T. 0200, Australia*

Received 19 November 2001; accepted 3 May 2002

Abstract

Monazite grains from Nepal and Vietnam were compositionally analyzed with an electron microprobe and dated (Th–Pb) with an ion microprobe. Five sources of uncertainty explain age distributions from single samples that appear inconsistent with a single population: (1) Pb loss due to diffusion, (2) dissolution/reprecipitation reactions along a retrograde path, (3) analytical uncertainties, (4) analyses of overlapping age domains, and (5) episodic monazite growth. The influence of these factors is sample-dependent, but can be evaluated: (1) using peak metamorphic conditions and X-ray element maps to assess potential polymetamorphism or retrogression, (2) obtaining other geochronologic data including previous work or dating other minerals in the sample, (3) evaluating any method-related uncertainty including counting statistics for electron microprobe analyses or calibration reproducibility for ion microprobe analyses, and (4) ascertaining the potential growth mechanism of the monazite grain including dissolution of detrital grains or production from rare earth element (REE) oxide or allanite. Chemical contents of monazite grains analyzed in this study fail to reflect timing information or mineral growth mechanisms. Instead of relying on monazite chemical composition, major (Mn, Fe, Mg, Ca) and minor (Y) element garnet-zoning patterns and peak $P–T$ conditions should be used to facilitate age interpretation. This thermobarometric data records the sample's thermal history, changes in garnet growth rate and mechanisms, and accessory mineral breakdown.

Keywords: Monazite; Ion microprobe; Geochronology; Metamorphic petrology; In situ dating

1. Introduction

Monazite (Ce, La, Th)PO_4 is frequently used to date igneous and metamorphic rocks. The mineral preferentially incorporates ThO_2 (e.g., Overstreet, 1967), sustains little radiation damage (e.g., Meldrum et al., 1998) and remains relatively impervious to Pb loss at high crustal temperatures (e.g., Smith and Giletti, 1997). Monazite appears in pelites near the garnet isograd (e.g., Smith and Barreiro, 1990; Harrison et al., 1997) and inclusions in garnet are armored against daughter product loss (e.g., Montel et al., 2000). Garnet-bearing assemblages allow the determination of pressure–temperature ($P–T$) conditions (e.g., Spear, 1993), and when combined with monazite age data, suggest a powerful combination for ascertaining the evolution of metamorphic terranes

* Corresponding author. School of Geology, 105 Noble Research Center, Oklahoma State University, Stillwater, OK, 74075, USA. Tel.: +1-405-744-9246; fax: +1-405-744-7841.
E-mail address: catlos@okstate.edu (E.J. Catlos).

0009-2541/02/$ - see front matter © 2002 Elsevier Science B.V. All rights reserved.
PII: S0009-2541(02)00099-2

(DeWolf et al., 1993; Harrison et al., 1997, 1998; Foster et al., 2000; Terry et al., 2000; Catlos et al., 2001; Gilley, 2001).

Numerous studies date monazite using an electron microprobe (e.g., Suzuki et al., 1994; Montel et al., 1996; Bindu et al., 1998; Braun et al., 1998; Cocherie et al., 1998; Finger et al., 1998; Crowley and Ghent, 1999; Williams et al., 1999; Martelat et al., 2000). The electron microprobe's detection limit for Pb hinders the utility of chemical age results (e.g., Olsen and Livi, 1998). Montel et al. (1996) suggest the technique is typically feasible for >100 Ma monazite with ±30–50 Ma precision and a total counting time of ~10 min.

An alternative approach is to date monazite in situ using an ion microprobe. Like electron microprobe analysis, the ion microprobe technique is nondestructive of textural relationships, analysis of small grains (~10 μm) and zones within larger grains is feasible, and results are available within a few minutes (e.g., Harrison et al., 1995). Precision is limited by the reproduction of a calibration curve, and is typically ±2% for Th–Pb ages (Harrison et al., 1995, 1999; Stern and Sanborn, 1998; Stern and Berman, 2000).

Despite promising developments using in situ methods, a primary issue remains unresolved for monazite geochronology: how to interpret the age data when results are inconsistent with a single population. This paper attempts to address this issue and provide a framework for those seeking to obtain and understand monazite ages from rocks using in situ techniques. Monazite grains from several localities in Nepal (Catlos, 2000) and Vietnam (Gilley, 2001) were dated using the ion microprobe. The 36 dated grains are found in 5 garnet + biotite + muscovite + plagioclase ± staurolite ± sillimanite-bearing metamorphic rocks. To examine if monazite major element chemical variability, including Y, La, Ce, Nd, Pr, Sm, and Gd, reflects timing (e.g., Ayers et al., 1999; Zhu and O'Nions, 1999a,b; Foster et al., 2000), compositional analyses were obtained from the dated grains using an electron microprobe. Examination of the textural relationships among minerals in these samples suggests important monazite-producing reactions can be speculated to occur. Additionally, garnet-zoning patterns and the peak P–T conditions are valuable pieces of information that facilitate age interpretation.

2. Monazite paragenesis

2.1. Monazite composition

High concentrations of Th and U coupled with low common Pb make monazite an ideal chronometer. ThO_2 contents vary from <1 to 30 wt.% (Overstreet, 1967), although 4–12 wt.% is a more common range (Deer et al., 1992; Stern and Sanborn, 1998). UO_2 wt.% in monazite is typically lower than ThO_2, and the mineral preferentially incorporates lighter rare earth elements (REE) over heavy REE (see compositions in Overstreet, 1967; Rapp and Watson, 1986; Montel, 1993; Pan, 1997; Finger et al., 1998; Zhu and O'Nions, 1999a,b; Broska et al., 2000; and this paper). Th enters the monazite structure through the coupled substitutions $Th^{4+}+Si^{4+}\rightarrow REE^{3+}+P^{5+}$, $Th^{4+}+Ca^{2+}\rightarrow 2REE^{3+}$, and $Th^{4+}+2Si^{4+}\rightarrow Ca^{2+}+2P^{5+}$ (e.g., Burt, 1989).

Monazite grains are typically zoned, and their compositions are invoked to explain changing environmental conditions during mineral growth (see Zhu and O'Nions, 1999b). Cressey et al. (1999) indicate that sector zoning in monazite is due to crystal chemical effects, and that specific grain surfaces discriminate against REE according to size. Monazite composition has been related to metamorphic grade (Overstreet, 1967; Bea and Montero, 1999; Pyle et al., 2001), but no correlation has been found as well (e.g., Kingsbury et al., 1993). Zhu and O'Nions (1999b) suggest that the bulk rock and source material from which the mineral crystallized control monazite composition.

Monazite compositions are important for geochronologists using ion microprobe analysis because the technique is standard-based, and a fundamental assumption is that the primary beam interacts similarly with the monazite age standard and unknown. Stern and Sanborn (1998) report that a high Th (>8 wt.%) monazite standard may lead to errors in measuring ages of low Th (<1 wt.%) grains. Additionally, an unidentified isobar complicates the determination of ^{204}Pb in monazite grains with moderate to high Th contents. This matrix effect issue is resolved by using standard grains with similar chemical compositions as unknowns and observations that monazite typically contains small amounts of common Pb (see Finger and Helmy, 1998).

Monazite composition has also been invoked as an important means for understanding the chemical evo-

lution of rocks that experienced a complicated metamorphic history. For example, in a study of Himalayan gneisses, Foster et al. (2000) surmises that lower Y concentrations in matrix monazites is clear evidence that the matrix grains crystallized at a later time than those included in the garnet. Finger and Helmy (1998) speculate that monazite grains with higher Y contents at the rims indicate crystal growth under prograde temperature conditions. Zhu and O'Nions (1999b) found significantly lower amounts of Y and heavy REE in monazite grains in rocks containing garnet as a major mineral compared to grains found in samples without garnet and those speculated to form after garnet breakdown. Pyle et al. (2001) found Y and heavy REE contents in monazite that coexist with xenotime to increase with rising temperature. These observations imply that monazite chemical composition may be exploited to address mechanisms and timing of monazite growth.

2.2. Monazite-forming reactions and stability

Table 1 lists several monazite-forming reactions. The applicability of these reactions to specific rocks has been speculated using textural observations and stoichiometry. The diverse list of reactions in this

Table 1
Monazite-forming reactions

Reactant[a]	Product[b]	H, M, I[c]	Source[d]
$REE(CO_3)F + H_3PO_4$ (*bastnäsite*)	$\rightarrow$ **REEPO$_4$** + HF + H_2O + CO_2 (*monazite*)	H	WS1975 G1996
$Ca_5(PO_4)_3F + 3REE(CO_3)F + H_2CO_3$ (*fluorapatite*)	$\rightarrow 3$**REEPO$_4$** + $5CaCO_3$ + 4HF	H	SHP1999
$Ca_5(PO_4)_3F + 3REE(CO_3)F + 6HF$	$\rightarrow 3$**REEPO$_4$** + 5CaF + $3H_2O + 3CO_2$	H	SHP1999
$Ca_{5-x}(REE_x)(P_{3-x}Si_x)O_{12}F +$ (*fluorapatite*) $(x-y)Ca^{2+} + 2(x-y)P^{5+} + 6(x-y)O^{2-}$	$\rightarrow (Ca_{5-y}REE_y)(P_{3-y}Si_y)O_{12}F + (x-y)$**REEPO$_4$** + $(x-y)SiO_2$	H, M	PFM1993a P1997
$Ca_{1-x}(REE_x)$(Ti, Al, Fe) SiO_4(O, OH, F) (*allanite*) $+(x-y)Ca^{2+} + 2(x-y)PO_4^{3-}$	$\rightarrow Ca_{1-y}$ (REE_y)(Ti, Al, Fe) SiO_4(O, OH, F)+$(x-y)$**REEPO$_4$**	H, M	PFM1993b P1997
Titanite+$(CO_3)^{2-}$+$(PO_4)^{3-}$ + F^- + OH^-	$\rightarrow$ **REEPO$_4$** + SiO_2 + calcite + rutile + epidote + bastnäsite + chlorite	H, M	PFM1993b P1997
(Ca, REE)$_2$(Al, Fe, Mg)Si_3O_{12}(OH) (*allanite*)	$\rightarrow$ **REEPO$_4$**	M	SB1990 SPSW2000
$3(M\text{-}HREE)_2O_3 + REE_2O_3 +$ (*in hornblende or* (*in allanite*) *titanite*) $2Ca_5(PO_4)_3(F, OH) + 6SiO_2$ (*apatite*)	$\rightarrow 6$**REEPO$_4$** + 6CaO 2Ca $(M\text{-}REE_3SiO_4)_3(F, OH)$ (*lessingite in apatite*)	M	BDH1996
$REEPO_4$ (old)	$\rightarrow$ **REEPO$_4$** (new)	M	AMGM1999 ZO1999a
$ThO_2 + REE_2O_3$ + Ce-poor $REEPO_4$	$\rightarrow$ **REEPO$_4$**	M	AGHR1993 KMWH1993
0.6chlorite + K^+ + $CaPO_4$ + $1.2SiO_2 + 3REE^{3+} + 0.4H^+$	$\rightarrow$ biotite + $5Ca_2^{+} + 3$ **REEPO$_4$** + $1.2H_2O$	M	LH1996
(LREE)Al_3 $(PO_4)_2(OH)_6$ (*florencite*)	$\rightarrow$ **REEPO$_4$** + H_2O	I	SBC1986
$CaPO_4 + Liq_1$ (*apatite*)	$\rightarrow$ **REEPO$_4$** + Liq_2	I	WL1995

[a] The minerals or substances participating in the monazite-forming reaction. Some mineral names are indicated in italics.
[b] Products, including monazite (bold $REEPO_4$), formed as a result of the reaction. In some cases, reactions are balanced.
[c] "H," hydrothermal, "M," metamorphic, or "I," igneous environments.
[d] References: AGHR1993, Akers et al. (1993); AMGM1999, Ayers et al. (1999); BDH1996, Bingen et al. (1996); G1996, Giere (1996); KMWH1993, Kingsbury et al. (1993); LH1996, Lanzirotti and Hanson (1996); PFM1993a, Pan et al. (1993a); PFM1993b, Pan et al. (1993b); P1997, Pan (1997); SBC1986, Sawka, et al. (1986); SPSW2000, Simpson et al. (2000); SHP1999, Smith et al. (1999); WS1975, Watson and Snyman (1975); WL1995, Wolf and London (1995); ZO1999a, Zhu and O'Nions (1999a).

table clearly indicates that monazite formation varies as a function of bulk rock composition and $P-T$ conditions (see Wing et al., 1999). Precursor minerals in prograde metamorphic rocks are allanite, apatite, REE and Th oxides (e.g., Smith and Barreiro, 1990; Kingsbury et al., 1993). Along the retrograde path, monazite has been identified as a replacement after allanite (Pan, 1997; Finger et al., 1998), as well as after preexisting monazite (e.g., Ayers et al., 1999; Townsend et al., 2000).

The reactions in Table 1 are empirical and are not experimentally calibrated, but petrographic and thermobarometric studies suggest that monazite appears in metapelites during prograde metamorphism at ~ 500–600 °C via allanite breakdown reactions (e.g., Smith and Barreiro, 1990; Ayers et al., 1999; Rubatto et al., 2001). These thermal conditions are coincident with the appearance of garnet in metamorphic assemblages (e.g., Spear, 1993), indicating that $P-T$ paths can be constrained with timing information (e.g., Tuccillo et al., 1992). Monazite inclusions in garnet are also protected from Pb loss (DeWolf et al., 1993; Zhu et al., 1997; Zhu and O'Nions, 1999a; Foster et al., 2000; Montel et al., 2000; Stern and Berman, 2000; Terry et al., 2000).

Fig. 1 is a schematic $P-T$ diagram for allanite, loosely based on the epidote stability field (e.g., Liou, 1973) and observations of the relationship of allanite and monazite in metamorphic rocks (e.g., Overstreet, 1967). Because allanite has the potential to accept more elements than epidote, we speculate that allanite is able to exist in a wider range of pressures and temperatures. Along the prograde $P-T$ path in Fig. 1, monazite appears via allanite breakdown, whereas along the retrograde path, monazite is affected by dissolution and reprecipitation reactions (e.g., Ayers et al., 1999). Townsend et al. (2000) suggests that these retrograde reactions can occur at temperatures as low as 400 °C.

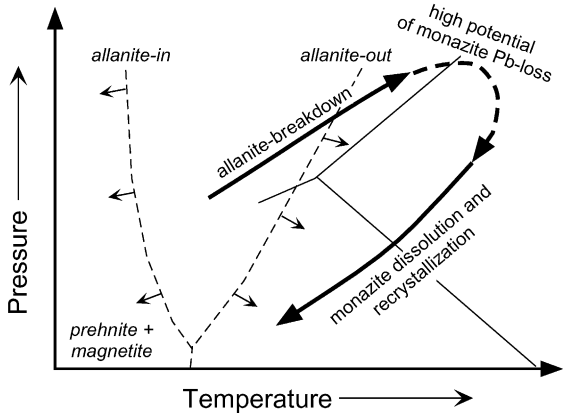

Fig. 1. Pressure–temperature ($P-T$) diagram outlining the speculated stability field of allanite, loosely based experiments with epidote (e.g., Liou, 1973) and observations allanite and monazite stability in metamorphic rocks (e.g., Overstreet, 1967). Monazite may form along the prograde leg of the $P-T$ path via allanite breakdown reactions (Table 1). Along the dashed leg, monazite may experience potential Pb loss due to elevated temperatures (e.g., Smith and Giletti, 1997). Along the retrograde path, monazite may sustain recrystallization or dissolution due to retrograde reactions (e.g., Townsend et al., 2000).

2.3. Monazite geochronology

Monazite has long been dated using the U–Pb method (e.g., Köppel, 1974; Köppel and Grünenfelder, 1975; Köppel et al., 1980; Schärer, 1984; Copeland et al., 1988) and more recently with Th–Pb systematics (Harrison et al., 1995; Edwards and Harrison, 1997; Harrison et al., 1997; Grove and Harrison, 1999; Murphy and Harrison, 1999; Townsend et al., 2000). Based on >700 compositional analyses, Overstreet (1967) reports that uranium rarely present in monazite in amounts >0.5 wt.%. Aliquots of monazite dated with the U–Pb system have the potential to produce ages with large uncertainties (see Nazarchuk, 1993; Hodges et al., 1996; Coleman, 1998; Möller et al., 2000 for examples). Problems could originate with the U–Pb method if the grains contain: (1) a significant inherited component (e.g., Copeland et al., 1988), (2) small amounts of U and Pb thereby meeting instrument limitations, or (3) excess ^{206}Pb from enrichments in ^{230}Th during crystal growth (Schärer, 1984; Parrish, 1990). External influences can also lead to greater uncertainty of monazite ages including: (1) Pb loss from prolonged experience above the closure temperature, (2) Pb loss due to a dissolution/reprecipitation process, or (3) incorporation of unsupported radiogenic ^{206}Pb or ^{207}Pb from included minerals such as uraninite or xenotime (e.g., Hawkins and Bowring, 1997). The benefits of an in situ method, including high spatial resolution and the small amount of material required for analysis, help to identify and overcome many of these issues, and

disequilibrium problems with U–Pb dating is resolved by using the Th–Pb system.

Early estimates for the closure temperature of Pb in monazite, dependent on grain size, diffusion coefficient, rate of cooling, were <650 °C (e.g., Wagner et al., 1977; Köppel et al., 1980; Black et al., 1984). Recent evidence, based primarily on studies of igneous and high-grade metamorphic rocks, suggests that monazite has a closure temperature of $\sim$ 700 to >800 °C (Copeland et al., 1988; Heaman and Parrish, 1991; Suzuki et al., 1994; Braun et al., 1998; Kamber et al., 1998). Smith and Giletti (1997) measured the tracer diffusion of Pb in natural monazites using ion microprobe depth profiling and observed Arrhenius parameters of $E=43\pm11$ kcal/mol and $D_o=6.6\times10^{-15}$ m^2/sec in the temperature range of 1200 to 1000 °C. In a Rutherford backscattering study of synthetic monazite grains, Cherniak et al. (2000) reports $E=149\pm9$ kcal/mol and $D_o=0.94$ m^2/sec at 1150 to 1350 °C. These strongly contrasting results may reflect intrinsic differences between natural and synthetic end-member monazite structures. Because the grains analyzed in this study are natural samples, we choose to use the values calculated by Smith and Giletti (1997) to evaluate their extent of diffusion. Note that the Cherniak et al. (2000) results would predict all the monazite grains to be more retentive for Pb under the peak temperature conditions experienced by the samples. Resolution of this issue may lie with the ion microprobe depth-profiling technique, a method to directly measure Pb loss within unpolished monazite grains (Grove and Harrison, 1999). Using this method, a continuous thermal history may be recovered for monazite grains separated from high-grade metamorphic rocks.

3. In situ ion microprobe sample preparation

Harrison et al. (1995, 1999) describe ion microprobe dating of monazite, whereas Zhu et al. (1997) briefly outline methods of in situ Secondary Ion Mass Spectrometry (SIMS) chronometry. Scherrer et al. (2000) develop procedures for obtaining monazite ages and compositions using an electron microprobe. We provide here technical details of the approach used for in situ ion microprobe monazite analysis. This methodology was specifically developed to obtain geochronologic and thermobarometric information from garnet- and monazite-bearing assemblages as the textural context of the grain being dated is preserved.

3.1. Petrographic analysis

Initially, uncovered rock thin sections are examined using an optical microscope. Petrographic analysis is especially important to identify mineral assemblages, garnet inclusion patterns, and extent of retrogression. The garnets analyzed here typically contain monazite, and we speculate that the mineral acts as a passive inclusion due to its low solubility under prograde conditions (e.g., Montel, 1986). During garnet growth, necessary elements are transported by diffusion to the surface of the porphyroblast. Minerals that do not participate in the reaction (e.g., zircon, monazite) or present in excess (e.g., biotite, plagioclase) are not removed completely and are overgrown (see Passchier and Trouw, 1996). Monazite inclusions may also result from local saturation of light REE, Th, or P near the margins of growing phenocrysts. The slow diffusion of these components away from the advancing crystal interface causes precipitation of monazite crystals, which are likely occluded (Harrison and Watson, 1984).

Monazite found on immobile grain boundaries may grow by Ostwald ripening, a process where large crystals grow at the expense of smaller crystals (Spear, 1993). Ostwald ripening is driven by the overall decrease in surface free energy resulting from consolidation of larger crystals, thereby reducing the total surface to volume ratio. Through time, the threshold size of dissolving grains increases, so that some crystals may initially grow, but then later shrink when the critical size is exceeded (Ayers et al., 1999). Monazite growth by Ostwald ripening has been observed by Kingsbury et al. (1993) in metapelites from the Mojave Desert, where monazite mean crystal size increases with increasing metamorphic grade.

3.2. Backscattered electron (BSE) imaging

For this study, the monazite grains found are typically too small ($\sim30-50$ μm) to be readily identified using optical petrography. Scherrer et al. (2000) suggest backscattered electron (BSE) imaging is the most efficient means to detect monazite. Mon-

azite grains are easily located due to their bright appearances and are qualitatively identified using an energy-dispersive X-ray detector. Fig. 2 shows BSE images of the ion microprobe monazite age standards (monazite 554; Harrison et al., 1999) obtained using a scanning electron microscope operating with an accelerating potential of 15 kV and a probe current of ~ 30 nA. Some zones within the monazite grains appear brighter, possibly correlating to higher ThO_2 content (~ 4 vs. ~ 3 wt.%; see Table 2). A spot on the darker area of the grain (#28) has the highest ThO_2 concentration, but the lowest $Sm_3O_2 + Gd_2O_3$ content, suggesting that the brightness relates to a complex interplay among heavy REE, Th and U (see also Cressey et al., 1999).

Monazite grains chosen for ion microprobe analysis are photographed at 50 × magnification to record their locations relative to major phases, and at 100 × or 200 × to record shapes and zoning. Detailed documentation is essential to ease relocating the grain using the optical systematics of the ion microprobe.

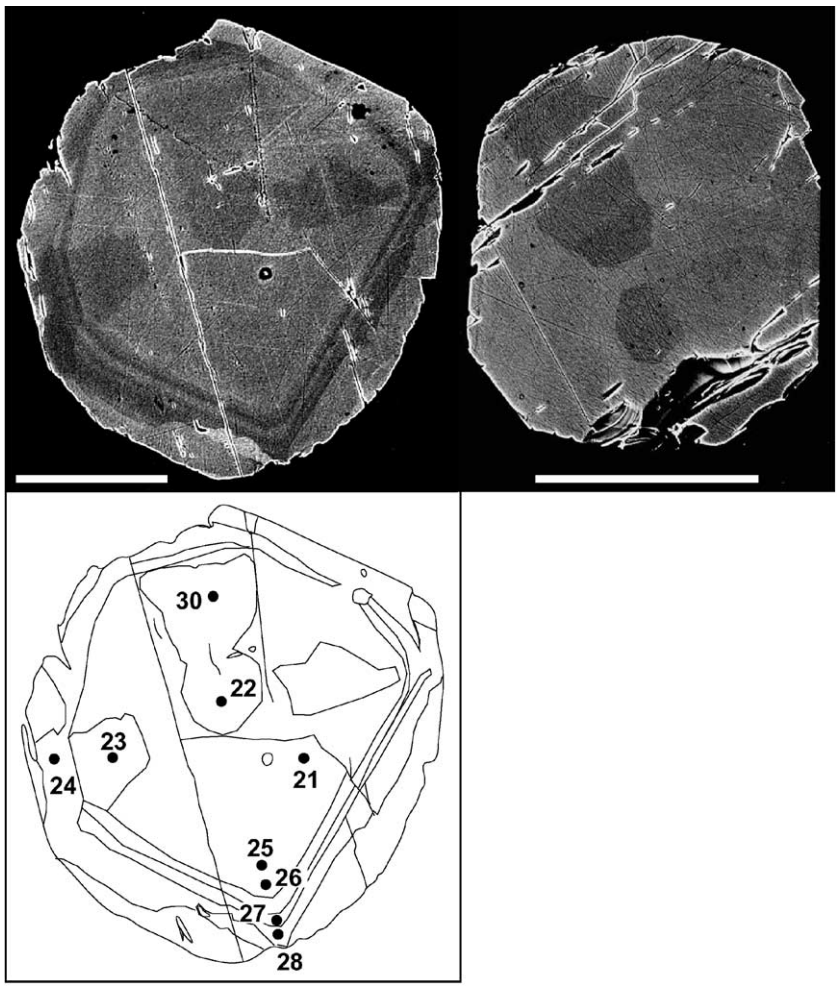

Fig. 2. (Upper) Backscattered electron microprobe images of monazite 554 grains, used as the age standard (see Harrison et al., 1995, 1999). Scale bars are 100 μm. (Lower) Map of the brightness zones of the left grain. Numbered black spots indicate areas where compositional analyses were taken (Table 2). The bright edges and cracks are artifacts of the high contrast necessary to enhance the zoning.

Table 2
Compositions of monazite 554[a]

Spot-brt[b]	21-L	25-L	26-L	27-L	22-D	23-D	30-D	28-D	24-VD
SiO_2	0.74	0.65	0.67	0.68	0.60	0.59	0.63	0.69	0.53
Al_2O_3	0.02	0.04	0.01	0.05	0.04	0.06	0.02	0.03	0.01
MgO	–[c]	–	–	–	0.02	–	–	–	0.01
CaO	1.01	1.00	1.19	1.21	0.94	1.01	1.07	1.23	0.99
Y_2O_3	1.29	1.03	1.67	1.31	1.25	1.10	1.15	1.79	1.66
ThO_2	4.15	3.80	3.91	4.26	3.00	2.93	3.87	4.31	2.90
La_2O_3	9.9	9.5	10.5	10.0	10.7	11.0	10.3	10.0	11.1
Ce_2O_3	24.6	25.7	24.7	24.4	24.4	25.4	24.9	24.1	25.6
Nd_2O_3	10.4	10.2	9.8	9.8	10.1	9.9	10.2	9.6	9.3
UO_2	0.02	0.11	0.09	0.08	0.02	0.01	–	0.12	0.01
Pr_2O_3	2.33	2.94	3.01	2.67	2.78	3.19	3.15	2.68	2.52
Sm_2O_3	1.27	1.32	1.11	1.23	1.12	1.17	1.09	1.02	1.14
Gd_2O_3	4.03	3.97	3.94	3.85	4.05	4.06	3.97	3.95	3.94
P_2O_5	30.5	29.9	30.1	30.1	30.0	30.2	30.4	30.3	29.7
Total[d]	90.3	90.1	90.7	89.6	89.0	90.5	90.7	89.7	89.3
Si	0.12	0.11	0.11	0.11	0.10	0.10	0.10	0.11	0.09
Al	<0.01	0.01	<0.01	0.01	0.01	0.01	<0.01	0.01	<0.01
Mg	<0.01	<0.01	<0.01	<0.01	<0.01	<0.01	<0.01	<0.01	<0.01
Ca	0.18	0.18	0.21	0.21	0.17	0.18	0.19	0.21	0.18
Y	0.11	0.09	0.15	0.11	0.11	0.10	0.10	0.16	0.15
Th	0.15	0.14	0.14	0.16	0.11	0.11	0.14	0.16	0.11
La	0.60	0.57	0.63	0.60	0.65	0.66	0.61	0.60	0.68
Ce	1.46	1.55	1.47	1.46	1.48	1.52	1.48	1.44	1.55
Nd	0.60	0.60	0.57	0.57	0.60	0.58	0.59	0.56	0.55
U	<0.01	<0.01	<0.01	<0.01	<0.01	<0.01	<0.01	<0.01	<0.01
Pr	0.14	0.18	0.18	0.16	0.17	0.19	0.19	0.16	0.15
Sm	0.07	0.07	0.06	0.07	0.06	0.07	0.06	0.06	0.06
Gd	0.22	0.22	0.21	0.21	0.22	0.22	0.21	0.21	0.22
P	4.19	4.16	4.15	4.18	4.19	4.16	4.18	4.18	4.16
Total[d]	7.8	7.9	7.9	7.9	7.9	7.9	7.9	7.9	7.9

[a] Monazite 554 is an ion microprobe age standard (see Harrison et al., 1999). Compositions normalized to 16 oxygens. Other elements not detected are Mg, Mn, and Ti. For operating conditions, see Catlos et al. (2000).

[b] Nomenclature is spot (see Fig. 2 for locations) and degree of brightness; "L," lighter, "D," darker, "VD," very dark areas.

[c] "–", analyzed but not detected.

[d] Low totals probably reflect incomplete analyses. Elements found in monazite 554 at levels>0.1 wt.%, but not analyzed here, include K_2O, ZrO_2, Dy_2O_3, and Er_2O_3 (Ken Livi, personal communication). Note that these analyses were conducted using the same standardization as the high quality allanite analyses reported by Catlos et al. (2000).

X-ray compositional maps of garnets in Mn, Ca, Fe, and Mg are acquired using an electron microprobe or scanning electron microscope to qualitatively evaluate garnet-zoning patterns. Garnets commonly show zoning that reflects growth events or diffusional modification (e.g., Spear, 1993; Spear and Kohn, 1996; Azor et al., 1997; Kohn et al., 1997), thus provide information about the integrated thermal history of the sample. The maps are also useful for identifying areas where compositional data should be obtained for thermobarometric calculations. Garnet X-ray maps of Y are also useful for deciphering the metamorphic history (Pyle and Spear, 1999).

3.3. Sample construction

The conductive coating is then removed from each thin section by abrasion, and the portions containing monazite, zircon, and minerals used for thermobarometry are cut out using a high-precision saw. The

fragments are cleaned with high-purity cleanser and mounted with a prepolished block of age standards on dual-sided tape. A 1-in. metallic ring is coated with release agent and placed around the thin section chips and age standards. Epoxy is then poured into the ring to a depth of ~10 mm. After the epoxy has hardened, the rings are broken away from the tape and the epoxy plugs are removed. The back of the plug is then cut to a desired thickness of ~5 mm. Fig. 3 is a typical in situ ion microprobe mount.

A reflected light image mosaic of the mount is then acquired using an optical microscope with a digital camera to facilitate location of monazite grains during ion microprobe analysis. The finished mount is then ultrasonically cleaned and coated with gold.

3.4. Ion microprobe analysis

Analytical procedures of ion microprobe Th–Pb dating of monazite (Harrison et al., 1995, 1999) are briefly summarized below. A 15–25-μm-diameter oxygen (O^-) primary beam with a primary intensity of 2 to 13 nA sputters positive ions from the surface of the sample. A mass resolving power of ~5000 is sufficient to separate molecular interferences and distinguish between Pb isotopes in the 204–208 mass range (Harrison et al., 1999). Typically, a 50 eV energy window with a 10 to 15 eV offset for $^{232}Th^+$ is used. The magnet is stepped through six different mass species: $^{204}Pb^+$, $^{207}Pb^+$, $^{208}Pb^+$, $^{232}Th^+$, ThO_2^+, and U^+. This cycle was repeated 15 times to correct for variations in beam stability, and average values were used to calculate ages.

Determination of the Pb/Th sensitivity factor is accomplished by dividing the measured $^{208}Pb^+/^{232}Th^+$ of a standard monazite at a reference ThO_2^+/Th^+ value by the standard's known daughter to parent ratio. The age of an unknown, measured under identical operating conditions, is determined by applying this sensitivity factor to the measured $^{208}Pb^+/^{232}Th^+$ value of the unknown. A calibration curve of ThO_2^+/Th^+ vs. $^{208}Pb^+/Th^+$ measured from a monazite standard is shown in Fig. 4. The reproducibility of the calibration line is the limiting factor on the precision of ion microprobe age determinations. All analyses in this study utilize monazite standard 554 (Fig. 2), a peraluminous granodiorite from the Santa Catalina Mountains in Arizona (Force, 1997). Th–Pb isotope

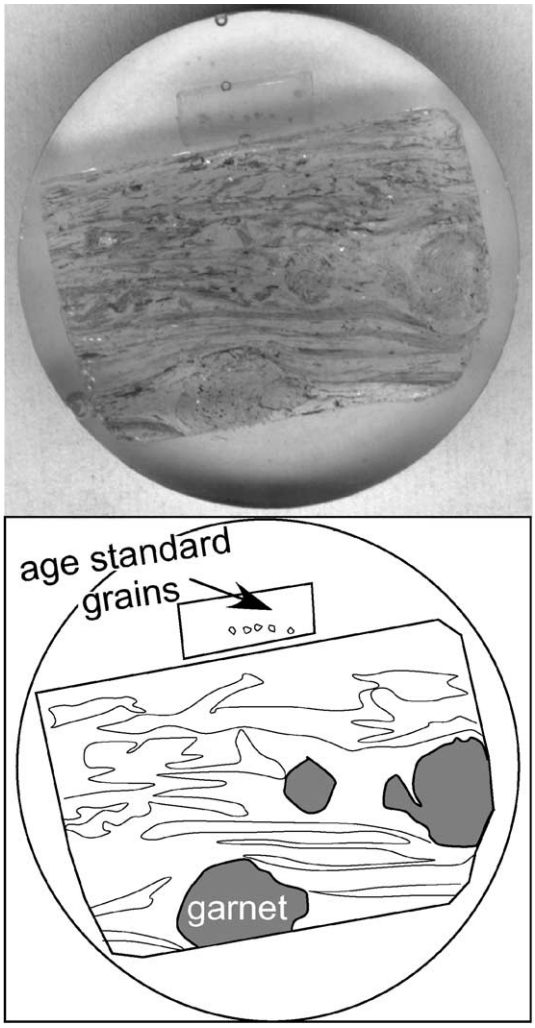

Fig. 3. (Upper) Photograph of a typical 1-in. diameter in situ ion microprobe mount and (lower) map of its components. The lower map outlines the block of monazite age standards and uncovered rock thin section. Rock foliation is indicated and garnet positions are shaded grey. Detailed reflected light photographs were taken of this sample to aid the monazite grain relocation process.

dilution analysis of 554 has produced radiogenic ^{208}Pb yields >98% and resulted in an age of 45.3 ± 1.4 Ma (2σ). This age is consistent with the 45 ± 1 Ma Th–Pb age determined by ion microprobe analysis (Harrison et al., 1999).

Monazite grains dated in situ are typically analyzed with one spot, limited by the size and irregular shape of the grain (typically <60-μm diameter) and primary

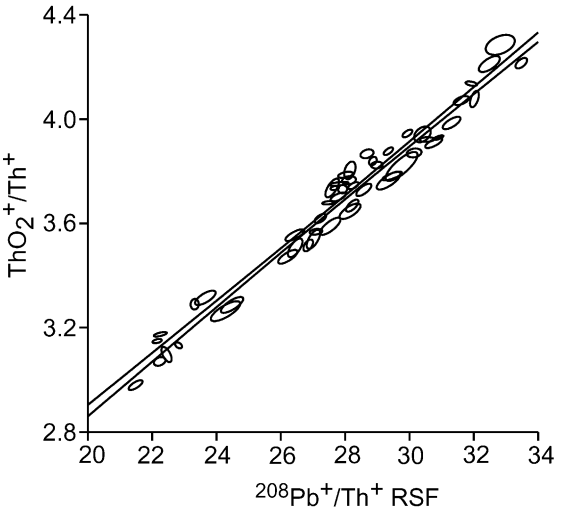

Fig. 4. Example of an ion microprobe calibration. RSF, Relative Sensitivity Factor. Ellipses represent isotopic data taken from spots on monazite 554. The slope is 0.102 ± 0.003 (1σ), intercept 0.836 ± 0.074, and correlation (r^2) is 0.995. Regression lines outline the 1σ confidence.

beam (typically ~ 25–30 μm), as well as the optical capabilities of the reflected light microscope attached to the ion microprobe. Two analyses are performed on each spot to identify any variation in age as the ion beam drilled deeper into the grain.

4. Interpretation of Th–Pb monazite age results

Garnet-bearing assemblages were collected from Nepal (sample 85H20g, Hubbard, 1989; samples ET26, ET33, MA33; Catlos et al., 2001, 2002) and Vietnam (sample V5; Gilley, 2001). The monazite grains in these rocks were dated using the in situ ion microprobe method and compositionally analyzed with an electron microprobe. Table 3 summarizes the ion microprobe data and Y contents of the dated monazite grains. Reported ages are corrected for common Pb using ^{204}Pb and an assumed ^{208}Pb/^{204}Pb=38.6 (Stacey and Kramers, 1975) and the analyzed monazite grains typically yield >90% radiogenic ^{208}Pb. The geologic significance of the numerical results, specific sample locations, BSE images of some dated monazite grains, and conditions and compositions used for thermobarometric analysis are reported elsewhere (Hubbard, 1989; Catlos, 2000; Catlos et al., 2001, 2002; Gilley, 2001). The errors for all parameters in the following sections, including ages, ThO_2^+/Th^+, and percent radiogenic ^{208}Pb, are quoted at the 1σ level.

Overall, three distinct age patterns of are observed in these samples: (1) monazite inclusions in garnet and matrix grains yield similar ages, (2) monazite inclusions in garnet are older than matrix grains, and (3) matrix monazite grains are both younger and older than inclusions in garnet. These three scenarios illustrate the protocol used for in situ monazite age interpretation.

4.1. Case 1: matrix monazites and inclusions in garnet yield similar ages (MSWD ~ 1.0)

Sample MA33 contains two monazite inclusions in the garnet rim that are similar in age to the matrix grain (Fig. 5; Tables 3 and 4). The rock contains garnet+biotite+chlorite+plagioclase+muscovite+allanite+monazite+ilmenite+quartz. Garnets in this sample are large (>2 mm) euhedral grains with allanite+quartz+ilmenite cores, but monazite+ilmenite are the only minerals present within 100 μm of the rim. Chlorite is only found adjacent to garnet. The matrix of this rock is predominantly comprised of quartz+muscovite+biotite+plagioclase that define a parallel, continuous foliation. The maximum P–T conditions experienced by this sample is ~ 6.5 kbar and ~ 560 °C, suggesting that monazite in this rock grew during prograde metamorphism and were occluded by the growing garnet. Samples with matrix monazites that retain most or all of their Pb may have cooled rapidly from peak temperature (e.g., Parrish, 1990) or experienced conditions below their closure temperature, so that thermally activated diffusive Pb loss does not have long to operate.

Sample ET33 is similar to MA33 in that the age of the garnet inclusion is within error of the ages of matrix grains, but ET33 experienced peak P–T conditions of ~ 720 °C and ~ 10 kbar. ET33 contains garnet+biotite+muscovite+plagioclase+apatite+chlorite+ilmenite+monazite+zircon. Garnets in this sample are rounded and contain inclusions of quartz+plagioclase+biotite+ilmenite+apatite+monazite+zircon and are found in close association with chlorite. Large

Table 3
Monazite ion microprobe age and isotopic data with electron microprobe Y contents

Sample (grain-spot)[a]	Monazite location[b]	Age (Ma) ($\pm\sigma$)	Y content (wt.%)[c]	ThO_2^+/Th^+ ($\pm\sigma$)[d]	^{208}Pb (%) ($\pm\sigma$)[e]	$^{208}Pb^*/Th^+$ ($\pm\sigma$) ($\times 10^{-4}$)[f]
MA33						
1-1	i	7.0 (0.4)	0.68, 0.24	4.720 (0.026)	86.8 (3.4)	3.444 (0.205)
3-1	i	6.3 (0.4)	0.30, 0.10	5.312 (0.025)	84.6 (4.8)	3.093 (0.190)
2-1	m	6.7 (0.1)	0.51, 0.19	4.222 (0.012)	90.5 (0.7)	3.337 (0.039)
MA33 Calibration: $(0.094 \pm 0.005)x+(1.292 \pm 0.158)$; $r^2=0.998$; $ThO_2^+/Th^+ = 4.470 \pm 0.249$[g]						
ET33						
1-1	i	16.4 (2.2)	0.64, 0.78, 0.68	4.941 (0.224)	88.8 (2.4)	8.104 (1.089)
2-1	m	15.7 (0.7)	0.95	5.480 (0.033)	93.7 (0.8)	7.770 (0.332)
2-2	m	15.1 (0.3)	0.95, 0.90	5.820 (0.031)	94.2 (0.9)	7.483 (0.153)
2-3	m	15.6 (1.0)	0.97, 0.99	5.970 (0.219)	94.4 (1.0)	7.703 (0.497)
3b-1	m	14.7 (1.8)	0.92, 0.32	5.555 (0.360)	91.0 (1.4)	7.299 (0.914)
3b-2	m	15.3 (1.3)	0.92, 0.77	4.983 (0.035)	92.6 (1.0)	7.552 (0.627)
3a-1	m	14.4 (0.9)	1.49, 0.44, 0.74, 1.03	5.259 (0.042)	83.6 (1.6)	7.116 (0.430)
4-1	m	15.1 (0.7)	0.94	5.421 (0.065)	94.2 (0.8)	7.460 (0.358)
4-2	m	15.7 (1.2)	1.21	5.111 (0.083)	94.4 (1.0)	7.749 (0.577)
5-1	m	17.1 (3.1)	0.77, 0.80	5.225 (0.284)	88.0 (1.4)	8.441 (1.513)
ET33 Calibration: $(0.077 \pm 0.016)x+(2.245 \pm 0.769)$; $r^2=0.999$; $ThO_2^+/Th^+ = 6.020 \pm 0.242$						
85H20g						
2-1	i	14.2 (1.1)	0.40, 0.41, .050	3.761 (0.061)	92.0 (6.7)	7.006 (0.554)
3-1	i	13.3 (1.7)	1.07, 1.40	3.100 (0.046)	87 (10)	6.602 (0.818)
1-1	m	10.6 (0.5)	1.80	1.695 (0.004)	85.2 (2.3)	5.264 (0.225)
1-2	m	10.0 (0.7)	1.45, 1.88	2.212 (0.009)	62.4 (3.8)	4.948 (0.329)
85H20g Calibration 1: $(0.135 \pm 0.004)x+(0.072 \pm 0.101)$; $r^2=0.999$; $ThO_2^+/Th^+ = 3.327 \pm 0.173$						
4-1	m	13.3 (0.6)	0.45	3.129 (0.016)	90.1 (2.8)	6.562 (0.283)
5-1	m	13.1 (1.1)	<0.01, 0.37	2.991 (0.025)	81.1 (5.8)	6.484 (0.537)
7-1	m	16.5 (1.8)	<0.01, 0.05, 1.46	2.628 (0.018)	90.5 (3.8)	8.180 (0.909)
85H20g Calibration 2: $(0.065 \pm 0.006)x+(1.861 \pm 0.137)$; $r^2=0.994$; $ThO_2^+/Th^+ = 3.430 \pm 0.171$						
V5						
6-1	i	52.1 (3.2)	2.17, 1.67	4.815 (0.022)	98.8 (0.2)	25.79 (1.60)
7-1	i	169 (3)	0.59, 1.96	5.641 (0.026)	99.1 (0.1)	83.76 (1.59)
8-1	i	66.3 (2.4)	2.23, 1.53	6.605 (0.038)	95.5 (0.5)	32.83 (1.21)
11-1	i	64.3 (1.7)	1.47, 2.33	6.203 (0.030)	92.1 (0.7)	31.86 (0.84)
12-1	i	43.5 (0.9)	–	5.590 (0.024)	96.4 (0.3)	21.55 (0.44)
13-1	i	48.9 (0.9)	0.23	5.791 (0.013)	96.5 (0.3)	24.22 (0.43)
14-1	i	75.3 (5.6)	1.30	8.019 (0.094)	93.2 (1.8)	37.32 (2.78)
1-1	m	29.4 (1.0)	0.42	6.543 (0.032)	96.4 (0.4)	14.54 (0.51)
2-1	m	25.1 (0.9)	0.92, 0.94	5.632 (0.074)	89.4 (2.5)	12.42 (0.44)
3-1	m	28.4 (2.0)	0.71	4.729 (0.027)	96.5 (0.4)	14.07 (0.97)
5-1	m	41.6 (1.3)	1.99, 1.47	5.322 (0.014)	96.3 (0.3)	20.58 (0.63)
9-1	m	23.0 (2.4)	–	5.661 (0.063)	56.0 (5.7)	11.38 (1.19)
V5 Calibration: $(0.097 \pm 0.020)+(1.477 \pm 0.872)$; $r^2=0.996$; $ThO_2^+/Th^+ = 8.504 \pm 2.024$						
ET26						
5-1	i	23.9 (0.4)	2.91, 0.79	8.263 (0.088)	98.1 (0.6)	11.83 (0.191)
10-1	i	436 (8)	1.20	8.730 (0.129)	99.2 (0.3)	217.9 (4.022)
7-1	i	45.8 (2.8)	3.00, 3.36	7.310 (0.117)	51.7 (2.6)	22.69 (1.397)
3-1	m	44.5 (0.9)	0.97	9.464 (0.096)	98.7 (0.6)	22.02 (0.440)
8-1	m	20.4 (0.6)	0.71, 1.28	8.030 (0.108)	93.4 (1.4)	10.12 (0.282)
2-1	m	18.2 (0.4)	0.77, 1.33	8.967 (0.056)	93.5 (1.5)	9.018 (0.187)
ET26 Calibration: $(0.088 \pm 0.004)x+(2.732 \pm 0.266)$; $r^2=0.999$; $ThO_2^+/Th^+ = 8.988 \pm 0.441$						

(>1 mm long) apatite grains are adjacent to matrix monazite. ET33 matrix grains experienced little Pb loss probably due to larger size. The degree of Pb loss decreases with larger grain sizes as the surface area to volume ratio changes and diffusional losses lower because of less opportunity for Pb exchange with the surrounding environment. In many cases, multiple ~ 25 μm ion microprobe spots were placed on each ET33 grain (Table 3). Y contents of the monazite inclusions within the garnets in both of these samples are in the range of the compositions of the matrix grains. For example, matrix monazite grains in MA33 contain 0.2–0.5 wt.% Y_2O_3, whereas the inclusion has 0.1–0.7 wt.% (Tables 3 and 4). Matrix grains in ET33 contain 0.3–1.5 wt.% Y_2O_3, and the inclusion in garnet has 0.6–0.8 wt.% (Tables 3 and 5). The REE patterns are also not useful for identifying any unique chemical change between inclusions and matrix monazite in these samples (Fig. 6).

Sample MA33 experienced a polymetamorphic history, evidenced by element mapping and the older ages of allanite (>250 Ma than the monazite) inclusions within the core (Catlos et al., 2000). Fig. 7 shows a BSE image and Mn, Ca, Mg, Fe, and Y X-ray maps of a garnet rim from sample MA33. Major element zoning, especially the Mn, indicates the rock has a polymetamorphic history. One Y increase (to ~ 710 ppm) begins immediately after a Fe and Mg increase and Ca decrease, and appears near the end of the tapering Mn. A second Y band shows no correlation with Mn, Ca, Mg, or Fe, but is within the 100 μm of the rim, the region where the monazite grains are located (Fig. 5). Pyle and Spear (1999) outline several possibilities that could result in the formation of Y annuli, including open-system fluid interaction, changes in garnet growth rate, and breakdown of Y-rich phases during growth, and prefer garnet resorption and renewed growth as the mechanism in staurolite-grade schists. The second stage garnet in MA33 could have formed via garnet breakdown elsewhere in the sample, leading to increased Y and a band formation within the rim. Based on textural observations of the proximity of the monazite grains to the outer Y increase, we speculate that the second outer band may have resulted due to allanite breakdown. Allanite probably existed in the matrix of this sample, but is now only preserved in garnet cores. Y from allanite breakdown could have been partitioned into the monazite and growing garnet. Note that xenotime is not observed in this sample.

4.2. Case 2: monazite inclusions in garnet are older than matrix monazites (MSWD≠ 1.0)

Samples 85H20g and V5 have monazite inclusions in garnet that are older than matrix grains (Table 3). V5 is a mylonitic micaschist composed mainly of quartz+biotite+K-feldspar+sillimanite with minor amounts of apatite+ilmenite+monazite+zircon. V5 garnet porphyroblasts are large (>4 mm), elongated parallel to the stretching lineation, and cores contain inclusions of quartz+biotite+sillimanite+ilmenite+rutile+monazite+zircon. Thick, nearly inclusion free rims surround the inclusion-rich cores. Biotite shear bands and asymmetric pressure shadows on garnets show evidence of ductile deformation. Matrix quartz shows no subgrain boundaries or undulose extinction and appears to be statically annealed during incorporation into growing garnet. Brittle fractures in garnet and sillimanite perpendicular to the foliation indicate late stage stretching.

Notes to Table 3:

[a] Nomenclature indicates the grain and spot, respectively, of the analyzed monazite.

[b] Monazite inclusion in garnet is designated as "i", whereas "m" indicates a matrix grain.

[c] Y contents in weight percent of spots on the dated monazite grain. See Tables 4–8 for the complete electron microprobe analyses. "–", not analyzed.

[d] Measured ratio in sample.

[e] Percent radiogenically derived ^{208}Pb.

[f] Corrected sample ratio assuming $^{208}Pb/^{204}Pb = 39.5 \pm 0.1$ (Stacey and Kramers, 1975).

[g] Calibration information: Sample name, best fit of the calibration to the equation of a line (slope * x + intercept) with $\pm 1\sigma$ uncertainty, correlation (r^2), and range of ThO_2^+/Th^+ ($\pm 1\sigma$) measured using monazite 554. Ideally, the unknown ThO_2^+/Th^+ lies within the ThO_2^+/Th^+ range defined by the standard.

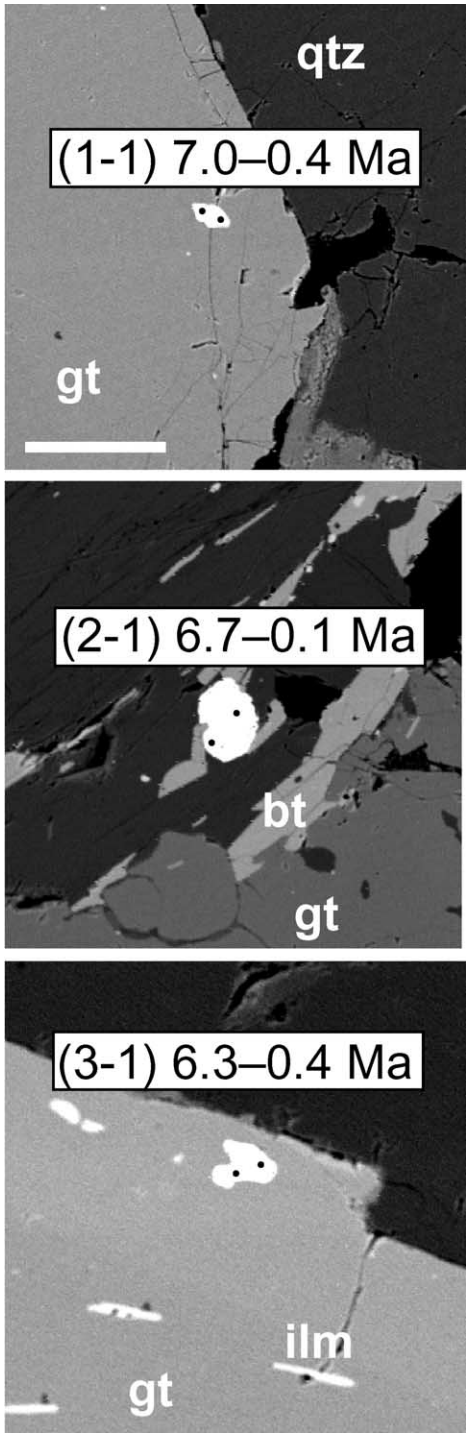

Table 4
MA33 monazite compositions and ages

Grain[a]	1[b]		2		3[b]	
Age, Ma[c]	7.0 (0.4)		6.7 (0.1)		6.3 (0.4)	
SiO_2	0.81	0.45	0.89	0.31	0.64	0.19
CaO	1.71	1.06	1.82	0.96	1.77	0.91
Y_2O_3	0.68	0.24	0.51	0.19	0.30	0.10
ThO_2	10.5	5.9	11.4	5.1	10.9	4.5
La_2O_3	13.0	15.2	12.9	13.5	12.7	13.4
Ce_2O_3	25.8	29.3	25.3	28.6	24.0	28.4
Nd_2O_3	11.4	12.5	11.5	13.3	10.6	12.9
UO_2	0.5	0.4	0.4	0.5	0.4	0.4
Pr_2O_3	3.07	3.18	3.25	3.76	2.90	3.32
Sm_2O_3	2.05	2.05	1.99	2.28	1.89	2.57
Gd_2O_3	1.80	1.34	1.61	1.22	1.53	1.50
P_2O_5	28.7	28.2	27.8	30.3	27.5	28.7
Total[d]	100	99.8	99.4	100	95.0	96.9
Si	0.13	0.07	0.14	0.05	0.11	0.03
Ca	0.29	0.18	0.31	0.16	0.32	0.16
Y	0.06	0.02	0.04	0.02	0.03	0.01
Th	0.38	0.22	0.42	0.18	0.41	0.17
La	0.76	0.90	0.77	0.78	0.78	0.80
Ce	1.50	1.73	1.50	1.63	1.47	1.69
Nd	0.65	0.72	0.66	0.74	0.63	0.75
U	0.02	0.01	0.02	0.02	0.02	0.01
Pr	0.18	0.19	0.19	0.21	0.18	0.20
Sm	0.11	0.11	0.11	0.12	0.11	0.14
Gd	0.09	0.07	0.09	0.06	0.08	0.08
P	3.86	3.84	3.80	4.00	3.88	3.96
Total[d]	8.0	8.1	8.1	8.0	8.0	8.0

[a] Number of the monazite grain analyzed by ion microprobe and electron microprobe.
[b] Monazite inclusion in garnet. Electron microprobe spots are indicated on the monazite grains in Fig. 5.
[c] Th–Pb ion microprobe age, Ma ($\pm 1\sigma$) of the monazite grain.
[d] Compositions normalized to 16 oxygen anions. Some poor totals may reflect incomplete analyses.

Sample 85H20g is lower grade than V5, comprised of sub- to euhedral garnets in contact with large (>2 mm long) staurolite grains. Garnets in the 85H20g metapelite vary in diameter from 500 μm to>2 mm

Fig. 5. BSE images of monazite grains dated and compositionally analyzed from sample MA33. Nomenclature indicates the grain number-ion microprobe spot. One ion microprobe spot could be focused on each grain. The black dots indicate where compositional data was taken using an electron microprobe. See Table 3 for isotopic data and Table 4 for compositions. Grains 1 and 3 are found as inclusions in garnet, whereas grain 2 is found in close association with biotite. Images are labeled: "qtz", quartz; "gt", garnet; "bt", biotite; "ilm", ilmenite. The scale bar, applicable to each image, is 100 μm.

Table 5
ET33 monazite compositions and ages

Grain[a]	1[b]				2				3A				3B				4		5	
Age, Ma[c]	16.4 (2.2)			15.7 (0.7)	15.1 (0.3)		15.6 (1.0)		14.4 (0.9)				14.7 (1.8)		15.3 (1.3)		15.1 (0.7)	15.7 (1.2)	17.1 (3.1)	
SiO_2	1.42	1.42	1.78	0.56	0.46	0.38	0.47	0.51	0.87	5.27	2.55	0.72	0.75	3.13	0.61	2.46	0.64	0.69	1.63	0.74
CaO	0.86	1.31	1.15	1.15	1.12	0.84	0.82	0.99	1.99	1.40	0.96	1.40	1.31	0.90	1.12	0.83	1.06	0.96	0.88	1.31
Y_2O_3	0.64	0.78	0.68	0.95	0.95	0.90	0.97	0.99	1.49	0.44	0.74	1.03	0.92	0.32	0.92	0.77	0.94	1.21	0.77	0.80
ThO_2	8.6	10.2	11.6	6.0	5.9	4.2	4.5	4.8	9.8	7.0	5.1	7.5	6.7	4.0	6.3	4.7	5.9	5.1	4.8	7.5
La_2O_3	14.8	14.7	13.6	14.5	14.3	15.4	14.5	14.8	12.8	12.4	13.6	13.4	14.2	11.8	15.0	11.9	14.0	13.4	14.6	13.9
Ce_2O_3	27.7	26.6	26.9	27.8	28.3	29.4	30.2	29.8	24.9	26.1	27.7	26.6	28.7	23.6	28.8	24.4	27.5	26.1	28.4	26.5
Nd_2O_3	12.1	11.5	11.1	12.7	12.1	12.3	13.1	12.1	11.2	10.8	12.5	11.8	11.7	10.6	11.9	11.6	11.9	12.0	12.5	11.8
UO_2	0.3	0.5	0.6	0.9	0.8	0.6	0.6	0.8	2.0	0.9	0.9	1.1	1.0	0.6	0.9	0.8	0.9	0.8	0.7	1.3
Pr_2O_3	2.95	2.95	2.88	3.35	3.49	3.17	3.13	3.03	2.63	2.65	3.58	3.10	3.00	2.76	3.23	3.09	2.73	3.23	3.58	3.07
Sm_2O_3	1.60	1.65	2.03	2.38	2.03	1.94	2.36	1.75	2.23	1.77	2.16	2.24	2.13	2.01	2.18	1.82	1.97	2.22	2.03	2.31
Gd_2O_3	1.25	1.37	0.75	1.96	1.82	0.98	1.59	1.66	1.51	0.90	1.33	1.49	1.39	0.64	1.14	1.40	1.47	1.31	1.41	1.96
P_2O_5	25.5	26.3	26.3	28.0	29.2	29.2	28.6	29.1	28.0	32.4	30.1	27.6	28.6	18.2	28.4	27.9	28.3	24.2	30.2	27.0
Total[d]	97.8	99.4	99.4	100	100	99.4	101	100	99.4	102	101	98.0	100	78.6	101	91.6	97.4	91.1	101	98.1
Si	0.24	0.23	0.29	0.09	0.07	0.06	0.07	0.08	0.14	0.74	0.38	0.12	0.12	0.66	0.10	0.40	0.10	0.12	0.25	0.12
Ca	0.15	0.23	0.20	0.20	0.19	0.14	0.14	0.17	0.34	0.21	0.15	0.25	0.22	0.20	0.19	0.15	0.19	0.19	0.14	0.23
Y	0.06	0.07	0.06	0.08	0.08	0.08	0.08	0.08	0.13	0.03	0.06	0.09	0.08	0.04	0.08	0.07	0.08	0.12	0.06	0.07
Th	0.33	0.38	0.43	0.22	0.21	0.15	0.16	0.17	0.36	0.22	0.18	0.28	0.24	0.19	0.23	0.18	0.22	0.21	0.17	0.28
La	0.92	0.89	0.82	0.86	0.83	0.90	0.85	0.86	0.76	0.64	0.76	0.81	0.83	0.92	0.88	0.72	0.84	0.89	0.82	0.85
Ce	1.70	1.60	1.61	1.64	1.64	1.71	1.75	1.72	1.46	1.34	1.53	1.59	1.67	1.81	1.68	1.47	1.63	1.72	1.58	1.60
Nd	0.72	0.67	0.65	0.73	0.68	0.70	0.74	0.68	0.64	0.54	0.67	0.69	0.66	0.80	0.67	0.68	0.69	0.77	0.68	0.69
U	0.01	0.02	0.02	0.03	0.03	0.02	0.02	0.03	0.07	0.03	0.03	0.04	0.04	0.03	0.03	0.03	0.03	0.03	0.02	0.05
Pr	0.18	0.18	0.17	0.20	0.20	0.18	0.18	0.17	0.15	0.14	0.20	0.18	0.17	0.21	0.19	0.19	0.16	0.21	0.20	0.18
Sm	0.09	0.09	0.11	0.13	0.11	0.11	0.13	0.09	0.12	0.09	0.11	0.13	0.12	0.15	0.12	0.10	0.11	0.14	0.11	0.13
Gd	0.07	0.07	0.04	0.10	0.09	0.05	0.08	0.09	0.08	0.04	0.07	0.08	0.07	0.04	0.06	0.08	0.08	0.08	0.07	0.11
P	3.63	3.66	3.64	3.80	3.89	3.92	3.84	3.89	3.80	3.83	3.83	3.82	3.84	3.24	3.83	3.88	3.89	3.68	3.88	3.77
Total[d]	8.1	8.1	8.1	8.1	8.03	8.0	8.1	8.0	8.1	7.9	8.0	8.1	8.1	8.3	8.1	8.0	8.0	8.2	8.0	8.1

[a] Number of the monazite grain analyzed by ion microprobe and electron microprobe.
[b] Monazite inclusion in garnet.
[c] Th–Pb ion microprobe age, Ma ($\pm 1\sigma$) of the monazite grain. In some cases (grains 2, 3B, and 4), more than one ion microprobe spot could be placed on the monazite grain.
[d] Compositions normalized to 16 oxygen anions. Some poor totals may reflect incomplete analyses.

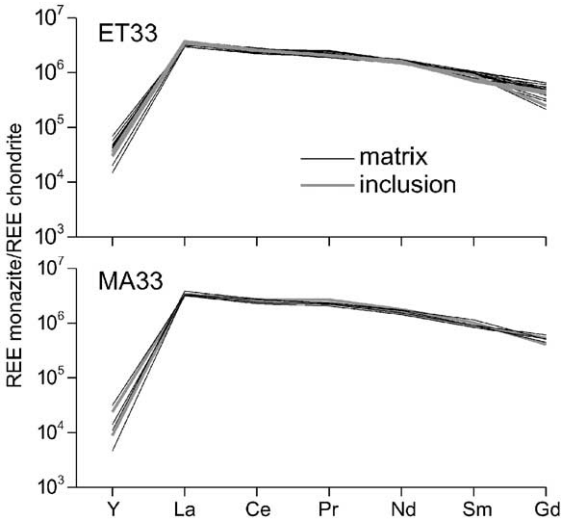

Fig. 6. Y+REE patterns from (upper) ET33 and (lower) MA33 monazite grains. Inclusions in garnet shown as grey and heavier line, whereas matrix grains are black. Compositions normalized using Anders and Grevesse (1989).

and have few scattered inclusions of ilmenite, quartz and monazite. Smaller garnet grains appear to overprint the foliation, whereas the larger grains are edged by symmetrical strain shadows of quartz, staurolite and mica. Chlorite mantles the edges of some garnet grains. The matrix of the rock contains staurolite+undulatory extinct quartz+biotite+muscovite+ilmenite+-monazite+zircon.

Several workers document the armoring properties of garnet, which shields monazite inclusions from reactions with other phases, diffusive Pb loss, recrystallization, or overgrowth (e.g., DeWolf et al., 1993; Poitrasson et al., 1996; Zhu and O'Nions, 1999a; Foster et al., 2000). Montel et al. (2000) suggests that minerals without prominent cleavage, such as garnet and quartz, act as the most efficient shields. These inclusions can time garnet growth or are detrital grains from a sedimentary or igneous protolith, or previous metamorphic cycle.

In rocks that experienced peak temperatures <650 °C, younger matrix monazite ages may reflect minor Pb loss or later growth. Experimental results reported by Smith and Giletti (1997) show that a 100-μm-diameter monazite held at 600 °C for 1 Ma retains 90% of its Pb. Sample 85H20g experienced maximum temperature of ~530 °C (Hubbard, 1989), coincident with the thermal conditions speculated necessary for monazite to appear in pelitic assemblages (Smith and Barreiro, 1990). The ~14 Ma grains within the garnet in this rock time their inclusion, whereas the ~10 Ma matrix monazite could represent continued mineral growth within the matrix. Diffusive Pb loss is excluded as a possibility because of thermal conditions experienced by this sample is insufficient to cause a ~14 Ma monazite grain to lose 29% of radiogenic ^{208}Pb, thereby yielding a ~10 Ma age. The precision of the younger ages (10.6 ± 0.5 and 10.0 ± 0.7 Ma) do not reflect a

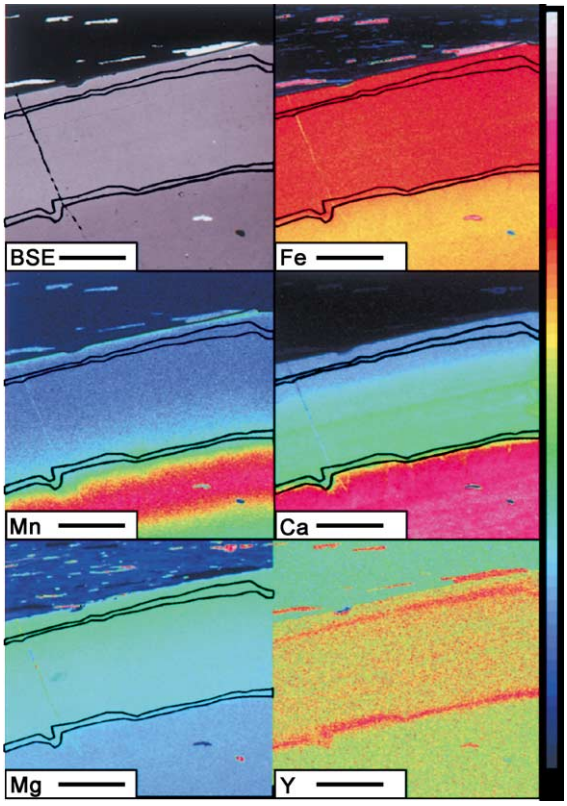

Fig. 7. BSE image and X-ray element maps of the garnet rim in sample MA33. The elements, Fe, Mn, Ca, Mg, and Y, respectively, and 100 μm scale bar are labeled at the bottom of the maps. The brightness scale ranges from a blue-black low to the magenta-pink high, and approximate locations of the two higher-Y bands overlay the BSE image element maps. The bright inclusion in the BSE image is ilmenite. These images were taken with the JEOL Superprobe at the University of Calgary.

method uncertainty, despite their ThO_2^+/Th^+ being out of the range defined by the calibration line (see Table 3). These mineral grains are less radiogenic ($85 \pm 2\%$ and $63 \pm 4\%$), so the younger ages may reflect variable amounts of common Pb contamination. Alternatively, younger matrix monazites could have grown via dissolution of preexisting monazite during later retrograde metamorphism that failed to affect other matrix grains due to their larger size or location. Retrograde fluid interaction is speculated to affect monazite grains at temperatures ~400 °C (Townsend et al., 2000).

If this pattern of ages is observed in samples that experienced high-temperature metamorphism (e.g., >650 °C), younger matrix monazite ages may be attributed to Pb loss. Smith and Giletti (1997) estimate that a 100-μm-diameter monazite heated to 650 °C for 1 Ma can sustain ~20% Pb loss, whereas if heated for 10 Ma, can experience ~50% Pb loss. Sample V5 experienced peak P–T conditions of ~800 °C and ~8 kbar (Gilley, 2001), indicating that the ~100×~20 μm-matrix monazite grains could be significantly affected by diffusive Pb loss. Note that the Cherniak et al. (2000) synthetic monazite diffusion study predicts only ~2% Pb loss for 20 μm monazite grains heated at 800 °C for 10 Ma, and negligible Pb loss at 600–650 °C, even for times extending to the age of the Earth. Resolution of these results may lie in ion microprobe

Table 6
V5 monazite compositions and ages

Grain[a]	1	2		3	5[b]		6[b]		7[b]		8[b]	11[b]			13[b]	14[b]
Age, Ma[c]	29.4 (1.0)	25.1 (0.09)		28.4 (2.0)	41.6 (1.3)		52.1 (3.2)		169 (3)		66.3 (2.4)	64.3 (1.7)			48.9 (0.9)	75.3 (5.6)
SiO_2	0.18	0.11	0.28	0.23	0.09	0.18	0.20	0.86	0.40	0.19	0.11	0.27	0.16	0.24	0.23	1.03
CaO	1.02	0.69	0.84	0.97	0.37	1.04	0.91	0.89	1.07	1.01	0.75	0.98	0.76	0.97	1.08	0.51
Y_2O_3	0.42	0.92	0.94	0.71	1.99	1.47	2.17	1.67	0.59	1.96	2.23	1.53	1.47	2.33	0.23	1.30
ThO_2	4.6	1.9	2.6	4.7	0.9	4.6	4.4	4.2	5.1	4.2	3.0	4.5	4.3	4.7	5.3	1.5
La_2O_3	14.3	13.1	13.4	14.4	15.8	13.7	14.1	14.4	14.3	13.9	14.4	14.7	12.8	13.5	14.8	14.7
Ce_2O_3	29.4	29.5	29.1	28.9	31.0	29.0	28.5	29.0	29.1	28.7	29.0	29.0	26.2	27.7	30.1	28.2
Nd_2O_3	12.5	14.9	13.1	12.8	12.8	12.2	12.2	12.8	12.6	11.9	12.7	11.6	10.8	12.7	12.2	10.8
UO_2	0.5	0.6	0.5	0.4	0.3	0.8	0.5	0.5	0.5	0.8	0.7	0.3	0.3	0.5	0.6	0.2
Pr_2O_3	3.46	3.89	3.50	3.69	3.75	3.05	3.12	3.64	3.67	3.46	3.18	3.14	2.97	3.19	3.28	3.21
Sm_2O_3	2.23	2.71	2.20	2.50	2.40	1.97	2.20	1.81	2.12	2.04	1.94	1.86	1.90	2.45	1.87	1.51
Gd_2O_3	1.46	1.79	1.69	1.45	1.46	1.88	1.86	2.06	1.29	1.45	1.64	1.09	1.25	1.77	1.40	0.99
P_2O_5	29.5	30.1	24.1	29.8	29.5	28.5	29.0	31.1	30.0	25.2	29.2	28.1	26.9	28.6	29.9	21.1
Total[d]	99.6	100	92.3	101	100	98.3	99.1	103	101	94.8	98.9	97.1	89.9	98.6	101	84.9
Si	0.03	0.02	0.05	0.04	0.01	0.03	0.03	0.13	0.06	0.03	0.02	0.04	0.03	0.04	0.04	0.20
Ca	0.17	0.12	0.16	0.16	0.06	0.18	0.15	0.14	0.18	0.19	0.13	0.17	0.14	0.17	0.18	0.11
Y	0.04	0.08	0.09	0.06	0.17	0.13	0.18	0.13	0.05	0.18	0.19	0.13	0.14	0.20	0.02	0.14
Th	0.17	0.07	0.11	0.17	0.03	0.17	0.16	0.14	0.18	0.17	0.11	0.17	0.17	0.17	0.19	0.07
La	0.84	0.75	0.89	0.83	0.92	0.82	0.83	0.80	0.82	0.89	0.84	0.88	0.82	0.80	0.85	1.06
Ce	1.71	1.69	1.92	1.66	1.79	1.71	1.66	1.59	1.66	1.83	1.69	1.74	1.67	1.63	1.72	2.02
Nd	0.71	0.83	0.84	0.72	0.72	0.70	0.69	0.68	0.70	0.74	0.72	0.68	0.67	0.73	0.68	0.76
U	0.02	0.02	0.02	0.01	0.01	0.03	0.02	0.02	0.02	0.03	0.02	0.01	0.01	0.02	0.02	0.01
Pr	0.20	0.22	0.23	0.21	0.21	0.18	0.18	0.20	0.21	0.22	0.18	0.19	0.19	0.19	0.19	0.23
Sm	0.12	0.15	0.14	0.13	0.13	0.11	0.12	0.09	0.11	0.12	0.11	0.10	0.11	0.14	0.10	0.10
Gd	0.08	0.09	0.10	0.07	0.08	0.10	0.10	0.10	0.07	0.08	0.09	0.06	0.07	0.09	0.07	0.06
P	3.95	3.98	3.67	3.95	3.92	3.90	3.91	3.95	3.95	3.70	3.94	3.89	3.97	3.89	3.96	3.51
Total[d]	8.0	8.0	8.2	8.0	8.1	8.1	8.0	8.0	8.0	8.2	8.0	8.1	8.0	8.1	8.0	8.3

[a] Number of the monazite grain analyzed by ion microprobe and electron microprobe.
[b] Monazite inclusion in garnet.
[c] Th–Pb ion microprobe age, Ma ($\pm 1\sigma$) of the monazite grain.
[d] Compositions normalized to 16 oxygen anions. Some poor totals may reflect incomplete analyses.

depth-profiling studies of unpolished monazite grains separated from sample V5 (e.g., Grove and Harrison, 1999).

Monazite inclusions in garnet in sample V5 also show considerable age range from 44 ± 1 to 169 ± 3 Ma (Table 3; see Gilley, 2001). To investigate whether the older ages represent a detrital signature, zircon inclusions in garnet and in the matrix were dated in situ in this same thin section. One zircon inclusion yields a concordant age of ~ 360 Ma, whereas the others were discordant and range from 550 to 750 Ma (Gilley, 2001). The metamorphic monazite in this rock may have formed from the dissolution of preexisting grains and some ages may represent overlapping analyses of detrital and metamorphic sections. In addition, only two of the monazite inclusions in garnet were not in contact with quartz in 2-D thin section view, leading to the hypothesis that quartz inclusions fail to armor these monazite grains from Pb loss under high-grade conditions. The 2-D thin section hinders the 3-D view of all the grains and unfortunately, the prograde garnet-zoning pattern in this sample has been completely eradicated via diffusion.

In previous studies (e.g., Foster et al., 2000), monazite Y content and REE patterns are used to distinguish between multiple episodes of monazite growth. However, electron microprobe analysis of monazites from samples V5 and 85H20g failed to

Table 7
85H20g monazite compositions and ages

Grain[a]	1			2[b]			3[b]		4	5		7		
Age, Ma[c]	10.6 (0.5)	10.0 (0.7)		14.2 (1.1)			13.3 (1.7)		13.3 (0.6)	13.1 (1.1)		16.5 (1.8)		
SiO_2	2.49	1.70	1.81	2.18	2.21	2.14	2.52	3.53	1.69	0.59	0.59	0.91	2.30	1.02
CaO	2.19	2.40	2.19	2.02	2.06	1.86	2.42	2.44	2.22	0.77	1.50	1.92	2.33	2.02
Y_2O_3	1.80	1.88	1.45	0.40	0.50	0.41	1.07	1.40	0.45	0.37	< 0.01	< 0.01	1.46	0.05
ThO_2	14.7	16.6	14.8	14.2	12.3	11.2	18.4	18.2	14.7	3.6	8.4	11.1	17.4	11.3
La_2O_3	10.2	10.7	11.7	12.0	12.4	12.5	11.0	10.6	12.7	16.0	15.6	13.8	11.6	13.6
Ce_2O_3	19.2	21.9	21.8	23.3	23.7	24.4	21.9	21.3	23.2	26.9	27.7	26.1	21.3	25.1
Nd_2O_3	9.3	9.0	9.3	9.9	10.2	9.8	9.0	8.6	9.4	11.4	11.2	10.7	8.1	10.6
UO_2	0.5	0.5	0.4	0.6	0.6	0.6	0.4	0.5	0.6	0.9	0.5	0.6	0.5	0.7
Pr_2O_3	2.52	2.29	2.43	2.62	2.37	2.42	2.63	2.67	2.75	2.90	3.08	3.10	2.11	2.96
Sm_2O_3	1.96	1.81	1.67	1.94	1.96	1.58	1.78	1.62	1.95	2.50	1.90	1.73	1.67	1.99
Gd_2O_3	2.28	2.06	2.24	1.79	1.52	1.78	2.38	1.97	1.54	1.13	0.77	1.05	2.65	1.20
P_2O_5	25.3	24.0	25.3	24.0	20.5	20.2	24.7	23.7	24.3	30.2	28.7	29.2	24.2	27.6
Total[d]	92.5	94.9	95.1	94.9	90.5	88.8	98.2	96.6	95.5	97.2	100	100	95.6	98.1
Si	0.42	0.30	0.31	0.38	0.42	0.41	0.42	0.59	0.29	0.09	0.09	0.14	0.39	0.17
Ca	0.40	0.45	0.40	0.37	0.42	0.38	0.43	0.44	0.41	0.13	0.26	0.32	0.43	0.35
Y	0.16	0.17	0.13	0.04	0.05	0.04	0.09	0.13	0.04	0.03	< 0.01	< 0.01	0.13	< 0.01
Th	0.57	0.66	0.57	0.56	0.53	0.49	0.70	0.70	0.58	0.13	0.30	0.40	0.68	0.42
La	0.64	0.68	0.73	0.76	0.86	0.88	0.68	0.66	0.81	0.93	0.91	0.80	0.73	0.82
Ce	1.20	1.39	1.36	1.48	1.64	1.72	1.34	1.32	1.46	1.55	1.62	1.50	1.33	1.50
Nd	0.56	0.56	0.56	0.61	0.69	0.67	0.53	0.52	0.58	0.64	0.64	0.60	0.49	0.61
U	0.02	0.02	0.02	0.02	0.03	0.03	0.02	0.02	0.02	0.03	0.02	0.02	0.02	0.03
Pr	0.16	0.14	0.15	0.16	0.16	0.17	0.16	0.16	0.17	0.17	0.18	0.18	0.13	0.18
Sm	0.12	0.11	0.10	0.12	0.13	0.10	0.10	0.09	0.12	0.14	0.10	0.09	0.10	0.11
Gd	0.13	0.12	0.13	0.10	0.10	0.11	0.13	0.11	0.09	0.06	0.04	0.05	0.15	0.06
P	3.65	3.54	3.63	3.52	3.28	3.28	3.50	3.38	3.56	4.03	3.87	3.88	3.51	3.80
Total[d]	8.0	8.1	8.1	8.1	8.3	8.3	8.1	8.1	8.1	7.9	8.0	8.0	8.1	8.1

[a] Number of the monazite grain analyzed by ion microprobe and electron microprobe.
[b] Monazite inclusion in garnet.
[c] Th–Pb ion microprobe age, Ma (± 1σ) of the monazite grain. More than one ion microprobe spot could be placed on the monazite grain 1.
[d] Compositions normalized to 16 oxygen anions. Some poor totals may reflect incomplete analyses.

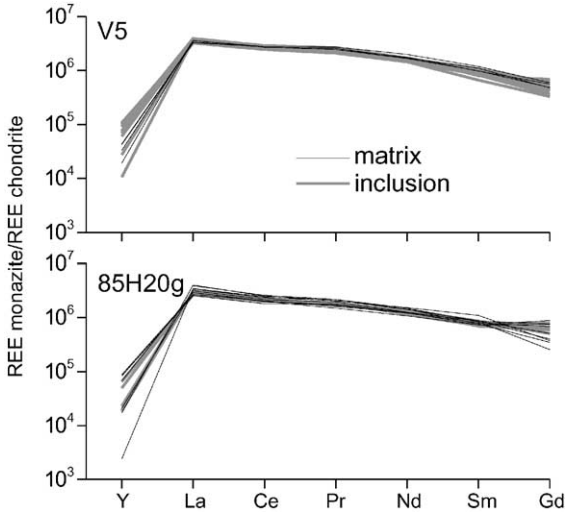

Fig. 8. Y + REE patterns from (upper) V5 and (lower) 85H20G monazite grains. Inclusions in garnet shown as grey and heavier line, whereas matrix grains are black. Compositions normalized using Anders and Grevesse (1989).

reveal any clear systematic trends in REE or Y compositions among matrix and inclusions, or among different age inclusions (Tables 6 and 7; Fig. 8). V5 matrix grains contain 0.4–0.9 wt.% Y_2O_3, whereas the inclusions have 0.2–2.3 wt.%. The oldest monazite inclusion contains 0.6–2.0 wt.% Y_2O_3, whereas the youngest garnet inclusion has 1.5–2.0 wt.%. In sample 85H20g, the youngest matrix grains contain 0.05–1.48 wt.% more Y_2O_3 than the inclusions. Although the ~ 10 Ma monazite grains could have grown after garnet, they contain higher Y contents. The observation is opposite that speculated by Foster et al. (2000), that significant depletions in Y in younger matrix monazites represent evidence that they crystallized after garnet inclusions. Y and REE content of monazites in these samples may just

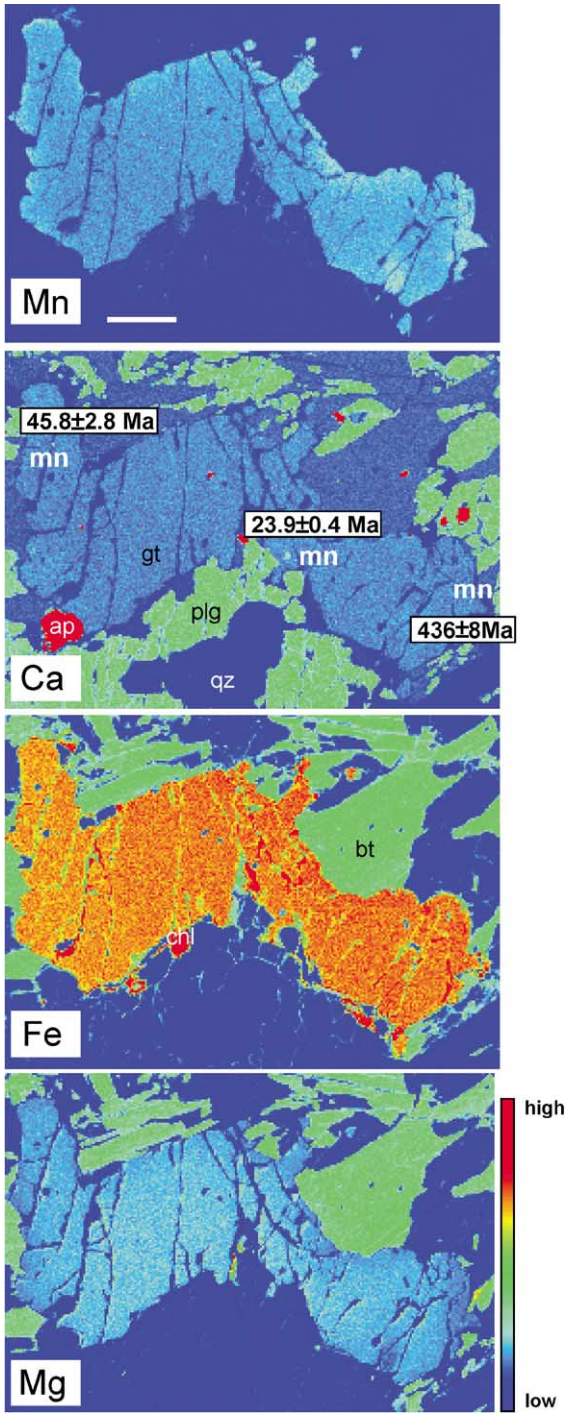

Fig. 9. X-ray element maps of a garnet in sample ET26. The elements, Mn, Ca, Fe, and Mg are labeled, and the scale bar is 200 μm. Th–Pb ages (± 1σ) are indicated on the Ca element map. See Table 3 for details of the geochronologic results and Table 8 for compositions of the dated grains. Images are labeled: "mon", monazite; "qz", quartz; "ap", apatite; "gt", garnet; "bt", biotite; "chl", chlorite.

reflect their crystallographic orientation (Cressey et al., 1999) and the grains dated by Foster et al. (2000) experienced high-grade metamorphism and most likely yield younger ages due to thermally activated Pb diffusion.

4.3. Case 3: matrix and included monazites yield range of ages (MSWD≠ 1.0)

A more complex case, where matrix and included monazite grains yield widely varying ages with no systematic age distribution pattern is observed in eastern Nepal sample ET26. This Himalayan rock contains garnet+chlorite+quartz+biotite+apatite+muscovite+ilmenite+monazite+zircon. Garnets in this rock are fragmented, in close association with chlorite, and some contain inclusions of biotite+rounded quartz+monazite+zircon. The matrix is predominantly comprised of undulatory extinct quartz and ~500-μm-long grains of thick biotite that define a spaced, rough foliation. Garnet zoning in this sample have been affected by significant diffusional relaxation, suggesting this rock as experienced high-temperature metamorphism (Fig. 9). The age range of monazite inclusions in ET26 may result from multiple episodes of garnet growth, but no clear core–rim relationships are deciphered from this fragmented garnet, using either petrological observations or X-ray element

Table 8
ET26 monazite compositions and ages

Grain[a]	2		3	5[b]		7[b]		8		10
Age, Ma[c]	18.2 (0.4)		44.5 (0.9)	23.9 (0.4)		45.8 (2.8)		20.4 (0.6)		436 (8)
SiO_2	0.37	0.37	2.00	0.24	0.22	0.22	0.29	0.23	0.24	0.58
CaO	1.47	1.37	1.31	1.45	1.53	1.39	1.31	1.52	1.46	1.21
Y_2O_3	0.77	1.33	0.97	2.91	0.79	3.00	3.36	0.71	1.28	1.20
ThO_2	6.6	6.6	5.9	6.1	6.8	6.3	5.9	7.1	6.5	6.1
La_2O_3	14.3	14.2	12.6	12.4	14.2	12.9	13.2	13.6	13.4	13.6
Ce_2O_3	28.2	27.4	25.9	25.1	28.5	26.5	25.9	27.3	27.3	27.1
Nd_2O_3	12.1	12.1	11.5	11.8	12.0	11.7	11.6	12.1	11.9	12.7
UO_2	0.8	0.8	0.9	1.1	0.9	0.9	1.0	0.9	0.8	0.4
Pr_2O_3	3.47	3.22	3.19	3.03	3.37	3.14	2.96	3.35	3.07	3.28
Sm_2O_3	2.16	1.85	2.04	2.18	1.87	2.11	1.81	2.10	2.20	2.38
Gd_2O_3	1.40	1.12	1.20	1.73	1.65	1.78	1.74	1.03	1.40	1.35
P_2O_5	29.2	28.8	28.9	31.7	27.8	29.5	28.5	30.2	29.6	29.2
Total[d]	101	99.2	96.6	99.8	99.5	99.5	97.6	100	99.2	99.1
Si	0.06	0.06	0.32	0.04	0.04	0.03	0.05	0.04	0.04	0.09
Ca	0.25	0.23	0.22	0.24	0.27	0.23	0.23	0.25	0.25	0.20
Y	0.06	0.11	0.08	0.24	0.07	0.25	0.29	0.06	0.11	0.10
Th	0.24	0.24	0.21	0.21	0.25	0.23	0.21	0.25	0.24	0.22
La	0.83	0.83	0.74	0.69	0.85	0.75	0.79	0.78	0.78	0.79
Ce	1.63	1.60	1.50	1.40	1.69	1.52	1.53	1.56	1.58	1.57
Nd	0.68	0.69	0.65	0.64	0.70	0.65	0.67	0.67	0.67	0.72
U	0.03	0.03	0.03	0.04	0.03	0.03	0.04	0.03	0.03	0.01
Pr	0.20	0.19	0.18	0.17	0.20	0.18	0.17	0.19	0.18	0.19
Sm	0.12	0.10	0.11	0.11	0.10	0.11	0.10	0.11	0.12	0.13
Gd	0.07	0.06	0.06	0.09	0.09	0.09	0.09	0.05	0.07	0.07
P	3.89	3.89	3.87	4.08	3.82	3.93	3.89	3.99	3.96	3.92
Total[d]	8.1	8.0	8.0	7.9	8.1	8.0	8.1	8.0	8.0	8.0

[a] Number of the monazite grain analyzed by ion microprobe and electron microprobe.
[b] Monazite inclusion in garnet.
[c] Th–Pb ion microprobe age, Ma ($\pm 1\sigma$) of the monazite grain.
[d] Compositions normalized to 16 oxygen anions. Some poor totals may reflect incomplete analyses.

mapping. As seen in samples describe in other case scenarios, no correlation between the age of these monazite inclusions and chemical contents are observed (Tables 3 and 8).

If garnet growth occurred in a single stage, two principal explanations produce the observed pattern: (1) the garnet incorporated monazites of varying age, perhaps grains from a sedimentary or igneous protolith and/or a preexisting metamorphic assemblage, or (2) monazites were the same age when they were incorporated by garnet, and have subsequently been reset. The armoring effect of garnet has been documented in numerous studies (e.g., Zhu and O'Nions, 1999a), arguing against partial resetting of monazite inclusions. If these inclusions were subjected to Pb loss, different parts of the garnet must have experienced different thermal histories, since the degree of resetting depends primarily on temperature and grain size. Fortunately, the ages of three monazite inclusions (436 ± 8, 45.8 ± 2.8, and 23.9 ± 0.4 Ma) in sample ET26 are documented in the Himalaya, and are linked to specific tectonic and metamorphic events (see Catlos et al., 2002). In view of these arguments, we accept the first scenario as a more plausible explanation for the wide age range observed in high-grade metamorphic rocks.

Gilley (2001) also observed the occurrence of similar sized monazite grains of Triassic to Oligocene age within a single garnet, but suggested that the age progression reflects overlapping analyses of two or more age domains. Unfortunately, optical limitations of the ion microprobe sometimes preclude precise positioning of the ion beam on specific domains within small (<30 μm) monazite grains during in situ analysis. BSE imaging or X-ray element mapping of larger monazite grains subsequent to ion microprobe analysis could resolve whether the ion beam spot overlapped age domains, if a chemical distinction relates to a different growth event.

5. Discussion and conclusions

Based on the geochronologic and compositional data set presented in this paper, we speculate that five mechanisms complicate the interpretation of monazite in situ analyses: (1) Pb loss due to prolonged experienced above the closure temperature (e.g., Smith and Giletti, 1997), (2) dissolution/reprecipitation along the retrograde path (e.g., Ayers et al., 1999), (3) analytical uncertainties, (4) analyses of overlapping age domains, and (5) episodic monazite growth.

The role that any of these factors in affecting the geochronologic results is sample-dependent, but can be evaluated. Peak metamorphic conditions and X-ray element maps are useful for assessing potential polymetamorphism or retrogression. Other geochronologic data, including previous work or dating other minerals (e.g., zircon) in the sample, can be used to evaluate the numerical results. Any method-related uncertainty should be explored including counting statistics for electron microprobe analyses or calibration reproducibility for ion microprobe analyses. The potential source of the monazite grain, including the dissolution of detrital grains or production from REE oxide or allanite, can be evaluated by detailed petrographic analysis of the sample or determining the protolith of the metamorphosed rock. Many monazite-producing reactions are invoked using only petrographic analyses and stoichiometry (Table 1; e.g., Simpson et al., 2000).

In this study, peak metamorphic conditions have been used to evaluate the extent of Pb loss possibly suffered by monazite that experienced high crustal thermal conditions using the parameters calculated for natural grains by Smith and Giletti (1997). However, the Cherniak et al. (2000) synthetic monazite diffusion study would predict that none of the monazite grains dated in this study would be significantly affected by Pb loss. To resolve this issue, monazite grains can be separated from the rock sample, mounted in epoxy as unpolished grains, and continuously analyzed using the ion microprobe depth-profiling technique. Using this method, Pb is directly measured within the sample; thus, a continuous thermal history for high-grade rocks can be recovered and evaluated (see Grove and Harrison, 1999).

Unfortunately, the chemical contents of the dated grains suggest that their temporal evolution is only conclusively determined through understanding their isotopic information. For example, the ion microprobe calibration standard, monazite 554, has a Th–Pb age of 45 ± 1 Ma (Harrison et al., 1999), but is chemically zoned (Fig. 2), cautioning that mineral zoning can be produced in shorter timescales than those resolvable using the ion microprobe. Furthermore, the REE

patterns and Y contents of many dated monazite grains in rocks that experienced different thermal histories are not useful to identify any specific growth mechanism. The temporal evolution of monazite growth and dissolution is only determined through geochronologic analysis.

Monazite REE-zoning patterns are applied as a means to better understand the mineral's reactions. Mohr (1984) describes zoning profiles of metamorphic monazites from North Carolina shales that show enrichment in Gd, Ce, Nd, and Sm and depletion in La and Y in monazite cores. Conversely, Finger et al. (1998) reports La content that decreases toward the rim in relict monazites that had experienced apatite replacement. Monazite composition may reflect crystal orientation, transfer of elements from the breakdown of REE phases under changing $P-T$ conditions, competitive crystallization among other REE phases, or replacement or recrystallization of an original grain during metamorphism (e.g., Cressey et al., 1999; Zhu and O'Nions, 1999b; Townsend et al, 2000; Pyle et al., 2001).

Instead of relying upon monazite chemical composition, garnet-zoning patterns and peak $P-T$ conditions can be used to facilitate age interpretation. The common occurrence of monazite as inclusions in garnet and observations that the garnet and monazite appear at conditions nearly coincident in temperature (i.e., ~ 500 °C; Smith and Barreiro, 1990), provides a unique opportunity to directly date prograde metamorphism. Thermobarometric data, including X-ray element maps, can assess the sample's potential polymetamorphism, retrogression, and in conjunction with diffusion studies (e.g., Smith and Giletti, 1997; Cherniak et al., 2000), maximum extent of monazite Pb loss. The garnet from sample MA33 indicates that X-ray maps of major and minor elements can be exploited to reveal a rock's polymetamorphic history and as a record accessory mineral breakdown (Fig. 7). Garnet can also protect monazite inclusions from subsequent Pb loss via diffusion or reactions with other phases. For example, Montel et al. (2000) propose that monazite inclusions in garnet are entirely disconnected from the rock matrix and can survive granulite facies conditions without being reset. Garnet inclusion patterns are also helpful for providing clues about changing metamorphic conditions during deformation (e.g., Passchier and Trouw, 1996).

The monazite grains analyzed in this study were found in rocks that experienced differing tectonic and thermal histories. Samples 85H20g and MA33 contain garnets that preserve growth zoning, but 85H20g contains younger grains in the matrix, suggesting retrograde reactions should be considered as a potential monazite growth mechanisms (e.g., Ayers et al., 1999). Samples ET33, ET26, and V5 contain garnets with zoning patterns characterized by diffusion, but monazites scattered throughout sample ET33 are of a single age population, consistent with grain size exerting an important control on Pb loss. In sample ET26, monazite inclusions of widely different age appear in a fragmented garnet and $P-T$ conditions are unrecoverable. However, in this scenario, the ages could be linked to specific tectonic and magmatic events reported for the Himalayan range.

With the advent of studies involving monazite diffusive Pb loss (e.g., Smith and Giletti, 1997; Cherniak et al., 2000), monazite mineral chemistry (e.g., Cressey et al., 1999), porphyroblast petrographic observations (e.g., Passchier and Trouw, 1996), thermobarometric calculations (e.g., Spear and Peacock, 1989), the potential exists for in situ dating to have widespread application. Combining monazite ages and thermobarometric constraints is a powerful method of obtaining a tectonic history. A rock is temporally constrained at depth within the Earth, and its exhumation rate can be calculated. A garnet rim $P-T$ data allows an evaluation of the amount of Pb diffusion possibly suffered by the monazite grain, whereas the age of an inclusion can be placed along an estimated $P-T$ path. In situ monazite ages are unaffected by problems plaguing studies that rely on mineral separation. The spatial resolution of the ion microprobe or electron microprobe instrumentation allows radiogenic-bearing minerals near or in contact with the monazite grain to be avoided, and the metamorphic and/or magmatic history of rocks can be obtained.

Acknowledgements

Funding from the National Science Foundation supported this project, and we acknowledge facility support from the Instrumentation and Facilities Program of the National Science Foundation. The

manuscript benefited greatly from comments by Drs. D.J. Cherniak, R.L. Rudnick, and an anonymous reviewer. **[RR]**

References

Akers, W.T., Grove, M., Harrison, T.M., Ryerson, F.J., 1993. The instability of rhabdophane and its unimportance in monazite paragenesis. Chem. Geol. 110, 169–176.

Anders, E., Grevesse, N., 1989. Abundances of the elements. Geochim. Cosmochim. Acta 53, 197–214.

Ayers, J.C., Miller, C., Gorisch, B., Milleman, J., 1999. Textural development of monazite during high-grade metamorphism: Hydrothermal growth kinetics, with implications for U, Th–Pb geochronology. Am. Mineral. 84, 1766–1780.

Azor, A., Simancas, J.F., Exposito, I., Lodeiro, F.G., Poyatos, D.J.M., 1997. Deformation of garnets in a low-grade shear zone. J. Struct. Geol. 19, 1137–1148.

Bea, F., Montero, P., 1999. Behavior of accessory phases and redistribution of Zr, REE, Y, Th, and U during metamorphism and partial melting of metapelites in the lower crust; an example from the Kinzigite Formation of Ivrea-Verbano, NW Italy. Geochim. Cosmochim. Acta 63, 1133–1153.

Bindu, R.S., Yoshida, M., Santosh, M., 1998. Electron microprobe dating of monazite from the Chittikara Granulite, South India; evidence for polymetamorphic events. J. Geosci. 41, 77–83.

Bingen, B., Demaiffe, D., Hertogen, J., 1996. Redistribution of rare earth elements, thorium, and uranium over accessory minerals in the course of amphibolite to granulite facies metamorphism: the role of apatite and monazite in orthogneisses from southwestern Norway. Geochim. Cosmochim. Acta 60, 1341–1354.

Black, L.P., Fitzgerald, J.D., Harley, S.L., 1984. Pb isotopic composition, colour and microstructure of monazites from a polymetamorphic rock in Antarctica. Contrib. Mineral. Petrol. 85, 141–148.

Braun, I., Montel, J.-C., Nicollet, C., 1998. Electron microprobe dating of monazites from high-grade gneisses and pegmatites of the Kerala Khondalite Belt, southern India. Chem. Geol. 146, 65–85.

Broska, I., Petrík, I., Williams, C.T., 2000. Coexisting monazite and allanite in peraluminous granitoids of the Tribec Mountains, Western Carpathians. Am. Mineral. 85, 22–32.

Burt, D.M., 1989. Compositional and phase relations among rare earth element minerals. In: Lipin, B.R., McKay, G.A. (Eds.), Geochemistry and Mineralogy of Rare Earth Elements, vol. 21. Mineralogical Society of America Reviews in Mineralogy, Washington, D.C., pp. 59–307.

Catlos, E.J., 2000. Geochronologic and thermobarometric constraints on the evolution of the Main Central Thrust, Himalayan orogen. PhD dissertation, University of California, Los Angeles, USA.

Catlos, E.J., Sorensen, S.S., Harrison, T.M., 2000. Th–Pb ion-microprobe dating of allanite. Am. Mineral. 85, 633–648.

Catlos, E.J., Harrison, T.M., Kohn, M.J., Grove, M., Ryerson, F.J., Manning, C.E., Upreti, B.N., 2001. Geochronologic and thermobarometric constraints on the evolution of the Main Central Thrust, central Nepal Himalaya. J. Geophys. Res. 106, 16177–16204.

Catlos, E.J., Harrison, T.M., Manning, C.E., Grove, M., Rai, S.M., Hubbard, M.S., Upreti, B.N., 2002. Records of the evolution of the Himalayan orogen from in situ Th–Pb ion microprobe dating of monazite: Eastern Nepal and Garhwal. J. Asian Earth Sci. 20, 459–479.

Cherniak, D.J., Watson, E.B., Harrison, T.M., Grove, M., 2000. Pb diffusion in monazite: a progress report on a combined RBS/SIMS study. EOS Trans. 81, 25. Spring Suppl.

Cocherie, A., Legendre, O., Peucat, J.J., Kouamelan, A.N., 1998. Geochronology of polygenetic monazites constrained by in situ electron microprobe Th–U-total lead determination: implications for lead behaviour in monazite. Geochim. Cosmochim. Acta 62, 2475–2497.

Coleman, M.E., 1998. U–Pb constraints on Oligocene–Miocene deformation and anatexis within the central Himalaya, Marsyandi Valley, Nepal. Am. J. Sci. 298, 553–571.

Copeland, P., Parrish, R.R., Harrison, T.M., 1988. Identification of inherited radiogenic Pb in monazite and its implications for U–Pb systematics. Nature 333, 760–763.

Cressey, G., Wall, F., Cressey, B.A., 1999. Differential REE uptake by sector growth of monazite. Mineral. Mag. 63, 813–828.

Crowley, J.L., Ghent, E.D., 1999. An electron microprobe study of the U–Th–Pb systematics of metamorphosed monazite: the role of Pb diffusion versus overgrowth and recrystallization. Chem. Geol. 157, 285–302.

Deer, W.A., Howie, R.A., Zussman, J., 1992. An Introduction to the Rock-Forming Minerals, 2nd ed. Longman Scientific and Technical Press, United Kingdom, 696 pp.

DeWolf, C.P., Belshaw, N., O'Nions, R.K., 1993. A metamorphic history from micron-scale $^{207}Pb/^{206}Pb$ chronometry of Archean monazite. Earth Planet. Sci. Lett. 120, 207–220.

Edwards, M.A., Harrison, T.M., 1997. When did the roof collapse? Late Miocene north–south extension in the High Himalaya revealed by Th–Pb monazite dating of the Khula Kangri granite. Geology 25, 543–546.

Finger, F., Helmy, H.M., 1998. Composition and total-Pb model ages of monazite from high-grade paragneisses in the Abu Swayel area, southern Eastern Desert, Egypt. Mineral. Petrol. 62, 269–289.

Finger, F., Broska, I., Roberts, M.P., Schermaier, A., 1998. Replacement of primary monazite by apatite–allanite–epidote coronas in an amphibolite facies granite gneiss from the eastern Alps. Am. Mineral. 83, 248–258.

Force, E.R., 1997. Geology and mineral resources of the Santa Catalina Mountains, southeastern Arizona. Monographs in Mineral Science, vol. 1. Center for Mineral Resources, Tucson, AZ, pp. 1–135.

Foster, G., Kinny, P., Vance, D., Prince, C., Harris, N., 2000. The significance of monazite U–Th–Pb age data in metamorphic assemblages; a combined study of monazite and garnet chronometry. Earth Planet. Sci. Lett. 181, 327–340.

Giere, R., 1996. Formation of rare earth minerals in hydrothermal systems. In: Jones, A.P., Wall, F., Williams, C.T. (Eds.), Rare Earth Minerals: Chemistry, Origin, and Ore Deposits. Mineral. Soc. Ser., vol. 7. Chapman & Hall, England, pp. 105–150.

Gilley, L., 2001. Timing of left-lateral shearing and prograde metamorphism along the Red River Shear Zone, China and Vietnam. Master's Thesis, University of California, Los Angeles, U.S.A.

Grove, M., Harrison, T.M., 1999. Monazite Th–Pb age depth profiling. Geology 27, 487–490.

Harrison, T.M., Watson, E.B., 1984. The behavior of apatite during crustal anatexis: equilibrium and kinetic considerations. Geochim. Cosmochim. Acta 48, 1467–1477.

Harrison, T.M., McKeegan, K.D., Le Fort, P., 1995. Detection of inherited monazite in the Manaslu leucogranite by $^{208}Pb/^{232}Th$ ion microprobe dating: crystallization age and tectonic implications. Earth Planet. Sci. Lett. 133, 271–282.

Harrison, T.M., Grove, M., Lovera, O.M., 1997. New insights into the origin of two contrasting Himalayan granite belts. Geology 25, 899–902.

Harrison, T.M., Grove, M., Lovera, O.M., Catlos, E.J., 1998. A model for the origin on Himalayan anatexis and inverted metamorphism. J. Geophys. Res. 103, 27017–27032.

Harrison, T.M., Grove, M., McKeegan, K.D., Coath, C.D., Lovera, O.M., Le Fort, P., 1999. Origin and emplacement of the Manaslu intrusive complex, Central Himalaya. J. Petrol. 40, 3–19.

Hawkins, D.P., Bowring, S.A., 1997. U–Pb systematics of monazite and xenotime: case studies from the Paleoproterozoic of the Grand Canyon, Arizona. Contrib. Mineral. Petrol. 127, 87–103.

Heaman, L., Parrish, R.R., 1991. U–Pb geochronology of accessory minerals. In: Heaman, L., Ludden, J.N. (Eds.), Applications of Radiogenic Isotope Systems to Problems in Geology. Mineralogical Association of Canada, Handbook, Toronto, ON, pp. 59–102.

Hodges, K.V., Parrish, R.R., Searle, M.P., 1996. Tectonic evolution of the central Annapurna Range, Nepalese Himalayas. Tectonics 15, 1264–1291.

Hubbard, M.S., 1989. Thermobarometric constraints on the thermal history of the Main Central Thrust Zone and Tibet Slab, eastern Nepal Himalaya. J. Metamorph. Geol. 7, 19–30.

Kamber, B.S., Frei, R., Gibb, A.J., 1998. Pitfalls and new approaches in granulite chronometry: an example from the Limpopo Belt, Zimbabwe. Precambrian Res. 91, 269–285.

Kingsbury, J.A., Miller, C.F., Wooden, J.L., Harrison, T.M., 1993. Monazite paragenesis and U–Pb systematics in rocks of the eastern Mojave Desert, California, U.S.A.: implications for thermochronometry. Chem. Geol. 110, 147–167.

Kohn, M.J., Spear, F.S., Valley, J.W., 1997. Dehydration-melting and fluid recycling during metamorphism: rangeley formation, New Hampshire, U.S.A. J. Petrol. 38, 1255–1277.

Köppel, V., 1974. Isotopic U–Pb ages of monazites and zircons from the crust-mantle transition and adjacent units of the Ivrea and Cenari Zones (Southern Alps, Italy). Contrib. Mineral. Petrol. 43, 55–70.

Köppel, V., Grünenfelder, M., 1975. Concordant U–Pb ages of monazite and xenotime from the Central Alps and the timing of the high temperature Alpine metamorphism, a preliminary report. Schweiz. Mineral. Petrogr. Mitt. 55, 129–132.

Köppel, V., Günthert, A., Grünenfelder, M., 1980. Patterns of U–Pb zircon and monazite ages in polymetamorphic units of the Swiss Central Alps. Schweiz. Mineral. Petrogr. Mitt. 61, 97–119.

Lanzirotti, A., Hanson, G.N., 1996. Geochronology and geochemistry of multiple generations of monazite from the Wepawaug Schist, Connecticut, U.S.A.: implications for monazite stability in metamorphic rocks. Contrib. Mineral. Petrol. 125, 332–340.

Liou, J.G., 1973. Synthesis and stability relations of epidote, $Ca_2Al_2FeSi_3O_{12}(OH)$. J. Petrol. 14, 381–413.

Martelat, J.-E., Lardeaux, J.-M., Nicollet, C., Rakotondrazafy, R., 2000. Strain pattern and late Precambrian deformation history in southern Madagascar. Precambrian Res. 102, 1–20.

Meldrum, A., Boatner, L.A., Weber, W.J., Ewing, R.C., 1998. Radiation damage in zircon and monazite. Geochim. Cosmochim. Acta 62, 2509–2520.

Mohr, D.W., 1984. Zoned porphyroblasts of metamorphic monazite in the Anakeesta Formation, Great Smoky Mountains, North Carolina. Am. Mineral. 69, 98–103.

Möller, A., Mezger, K., Schenk, V., 2000. U–Pb dating of metamorphic minerals: Pan-African metamorphism and prolonged slow cooling of high pressure granulites in Tanzania, East Africa. Precambrian Res. 104, 123–146.

Montel, J.-M., 1986. Experimental determination of the solubility of Ce-monazite in $SiO_2–Al_2O_3–K_2O–Na_2O$ melts at 800 °C, 2 kbar, under H_2O-saturated conditions. Geology 14, 659–662.

Montel, J.-M., 1993. A model for monazite/melt equilibrium and application to the generation of granitic magmas. Chem. Geol. 110, 127–146.

Montel, J.-M., 1999. Some good reasons for monazite to be concordant. European Union Geosciences 10. J. Conf. Abstr. 4, 800.

Montel, J.-M., Foret, S., Veschambre, M., Nicollet, C., Provost, A., 1996. Electron microprobe dating of monazite. Chem. Geol. 131, 37–53.

Montel, J., Kornprobst, J., Vielzeuf, D., 2000. Preservation of old U–Th–Pb ages in shielded monazite: example from Beni Bousera Hercynian kinzigites (Morocco). J. Metamorph. Geol. 18, 335–342.

Murphy, M.A., Harrison, T.M., 1999. Relationship between leucogranites and the Qomolangma Detachment in the Rongbuk Valley, South Tibet. Geology 27, 831–834.

Nazarchuk, J.H., 1993. Structure and geochronology of the Greater Himalaya, Kali Gandaki region, west-central Nepal, Masters Thesis, Carleton University, Ontario, Canada.

Olsen, S.N., Livi, K., 1998. Dating of monazite from migmatites in the Aar Massif, Swiss Alps, by electron microprobe analyses. Geol. Soc. Am. 1998 Annual Meeting Toronto, ON, Canada, Abstr. Progr. 30, 231.

Overstreet, W.C., 1967. The geologic occurrence of monazite. Geol. Surv. Prof. Pap. 530, 1–327.

Pan, Y., 1997. Zircon- and monazite-forming metamorphic reactions at Manitouwadge, Ontario. Can. Mineral. 35, 105–118.

Pan, Y., Fleet, M.E., MacRae, N.D., 1993a. Oriented monazite inclusions in apatite porphyroblasts from the Hemlo gold deposit, Ontario, Canada. Mineral. Mag. 57, 697–707.

Pan, Y., Fleet, M.E., MacRae, N.D., 1993b. Late alteration in titanite ($CaTiSiO_5$); redistribution and remobilization of rare earth elements and implications for U/Pb and Th/Pb geochronology and nuclear waste disposal. Geochim. Cosmochim. Acta 57, 355–367.

Parrish, R.R., 1990. U–Pb dating of monazite and its application to geological problems. Can. J. Earth Sci. 27, 1431–1450.

Passchier, C.W., Trouw, R.A.J., 1996. Microtectonics. Springer-Verlag, New York, 289 pp.

Poitrasson, F., Chenery, S., Bland, D.J., 1996. Contrasted monazite hydrothermal alteration mechanisms and their geochemical implications. Earth Planet. Sci. Lett. 145, 79–96.

Pyle, J.M., Spear, F.S., 1999. Yttrium zoning in garnet: coupling of major and accessory phases during metamorphic reactions. Geol. Mater. Res. 1, 1–36.

Pyle, J.M., Spear, F.S., Rudnick, R.L., McDonough, W.F., 2001. Monazite–xenotime–garnet equilibrium in metapelites and a new monazite–garnet thermometer. J. Petrol. 42, 2083–2107.

Rapp, R.P., Watson, E.B., 1986. Monazite solubility and dissolution kinetics; implications for the thorium and light rare earth chemistry of felsic magmas. Contrib. Mineral. Petrol. 94, 304–316.

Rubatto, D., Williams, I.S., Buick, I.S., 2001. Zircon and monazite response to prograde metamorphism in the Reynolds Range, central Australia. Contrib. Mineral. Petrol. 140, 458–468.

Sawka, W.N., Banfield, J.F., Chappell, B.W., 1986. A weathering-related origin of widespread monazite in S-type granites. Geochim. Cosmochim. Acta 50, 171–175.

Schärer, U., 1984. The effect of initial ^{230}Th disequilibrium on young U–Pb ages: the Makalu case, Himalaya. Earth Planet. Sci. Lett. 67, 191–204.

Scherrer, N.C., Engi, M., Gnos, E., Jakob, V., Liechti, A., 2000. Monazite analysis; from sample preparation to microprobe age dating and REE quantification. Schweiz. Mineral. Petrogr. Mitt. 80, 93–105.

Simpson, R.L., Parrish, R.R., Searle, M.P., Waters, D.J., 2000. Two episodes of monazite crystallization during metamorphism and crustal melting in the Everest region of the Nepalese Himalaya. Geology 28, 403–406.

Smith, H.A., Barreiro, B., 1990. Monazite U–Pb dating of staurolite grade metamorphism in pelitic schists. Contrib. Mineral. Petrol. 105, 602–615.

Smith, H.A., Giletti, B.J., 1997. Lead diffusion in monazite. Geochim. Cosmochim. Acta 61, 1047–1055.

Smith, M.P., Henderson, P., Peishan, Z., 1999. Reaction relationships in the Bayan Obo Fe–REE–Nb deposit Inner Mongolia, China: implications for the relative stability of rare-earth element phosphates and fluorocarbonates. Contrib. Mineral. Pet. 134, 294–310.

Spear, F.S., 1993. Metamorphic Phase Equilibria And Pressure–Temperature–Time Paths Mineralogical Society of America, Washington, DC, 799 pp.

Spear, F.S., Kohn, M.J., 1996. Trace element zoning in garnet as a monitor of crustal melting. Geology 24, 1099–1102.

Spear, F.S., Peacock, S.M., 1989. Metamorphic pressure–temperature–time paths. Am. Geophys. Union Short Course Geol., vol. 7. American Geophysical Union, Washington, D.C., pp. 1–25.

Stacey, J.S., Kramers, J.D., 1975. Approximate of terrestrial lead isotope evolution by a two-stage model. Earth Planet. Sci. Lett. 26, 207–221.

Stern, R.A., Berman, R.G., 2000. Monazite U–Pb and Th–Pb geochronology by ion microprobe, with an application to in situ dating of an Archean metasedimentary rock. Chem. Geol. 172, 113–130.

Stern, R.A., Sanborn, N., 1998. Monazite U–Pb and Th–Ph geochronology by high-resolution secondary ion mass spectrometry. Radiogenic Age and Isotopic Studies, Report 11, Curr. Res. 1998-F. Geological Survey of Canada, Ottawa, ON, Canada, pp. 1–18.

Suzuki, K., Adachi, M., Kajizuka, I., 1994. Electron microprobe observations of Pb diffusion in metamorphosed detrital monazite. Earth Planet. Sci. Lett. 128, 391–405.

Terry, M.P., Robinson, P., Hamilton, M.A., Jercinovic, M.J., 2000. Monazite geochronology of UHP and HP metamorphism, deformation, and exhumation, Nordoyane, Western Gneiss Region, Norway. Am. Mineral. 85, 1651–1664.

Townsend, K.J., Miller, C.F., D'Andrea, J.L., Ayers, J.C., Harrison, T.M., Coath, C.D., 2000. Low temperature replacement of monazite in the Ireteba granite, Southern Nevada: geochronological implications. Chem. Geol. 172, 95–112.

Tuccillo, M.E., Mezger, K., Essene, E.J., Van der Pluijm, B.A., 1992. Thermobarometry, geochronology, and the interpretation of $P–T–t$ data in the Britt Domain, Ontario Grenville orogen, Canada. J. Petrol. 33, 1225–1259.

Wagner, G.A., Reimer, G.M., Jaeger, E., 1977. Cooling age derived by apatite fission track, mica Rb–Sr, and K–Ar dating: the uplift and cooling history of the central Alps. Mem. 1st Geol. Mineral., vol. 30. University of Padova, Padova, Italy, pp. 1–27.

Watson, M.D., Snyman, C.P., 1975. The geology and the mineralogy of the fluorite deposits at the Buffalo fluor-spar mine on Buffelsfontein, 347KR, Naboomspruit District. Trans. Geol. South Afr. 78, 137–151.

Williams, M.L., Jercinovic, M.J., Terry, M.P., 1999. Age mapping and dating of monazite on the electron microprobe: deconvoluting multistage tectonic histories. Geology 27, 1023–1026.

Wing, B.A., Ferry, J.M., Harrison, T.M., 1999. The age of andalusite and kyanite isograds in New England from Th–Pb ion microprobe dating of monazite. 1998 Annual Meeting Toronto, ON, Canada, Abstr. Progr., vol. 30. Geological Society of America, Boulder, CO, p. 27.

Wolf, M.B., London, D., 1995. Incongruent dissolution of REE- and Sr-rich apatite in peraluminous granitic liquids: differential apatite, monazite, and xenotime solubilities during anatexis. Am. Mineral. 80, 765–775.

Zhu, X.K., O'Nions, R.K., 1999a. Zonation of monazite in metamorphic rocks and its implications for high temperature thermochronology: a case study from the Lewisian terrain. Earth Planet. Sci. Lett. 171, 209–220.

Zhu, X.K., O'Nions, R.K., 1999b. Monazite chemical composition: some implications for monazite geochronology. Contrib. Mineral. Petrol. 137, 351–363.

Zhu, X.K., O'Nions, R.K., Belshaw, N.S., Gibb, A.J., 1997. Lewisian crustal history from in situ SIMS mineral chronometry and related metamorphic textures. Chem. Geol. 136, 205–218.